Research Paper

THEMED ISSUE: Active Margins in Transition—Magmatism and Tectonics through Time

GEOSPHERE

GEOSPHERE; v. 12, no. 3

doi:10.1130/GES01232.1

14 figures; 3 tables; 1 supplemental file

CORRESPONDENCE: joshua.schwartz@csun.edu

CITATION: Schwartz, J.J., Stowell, H.H., Klepeis, K.A., Tulloch, A.J., Kylander-Clark, A.R.C., Hacker, B.R., and Coble, M.A., 2016, Thermochronology of extensional orogenic collapse in the deep crust of Zealandia: Geosphere, v. 12, no. 3, p. 647–677, doi:10.1130/GES01232.1.

Received 10 July 2015
Revision received 8 January 2016
Accepted 4 March 2016
Published online 20 April 2016

Thermochronology of extensional orogenic collapse in the deep crust of Zealandia

Joshua J. Schwartz[1], Harold H. Stowell[2], Keith A. Klepeis[3], Andy J. Tulloch[4], Andrew R.C. Kylander-Clark[5], Bradley R. Hacker[5], and Matthew A. Coble[6]

[1]Department of Geology, California State University Northridge, Live Oak 1202, 18111 Nordhoff Street, Northridge, California 91330, USA
[2]Department of Geological Sciences, University of Alabama, 201 7th Avenue, Room 2003 Bevill Building, Tuscaloosa, Alabama 35487, USA
[3]Department of Geology, University of Vermont, Delehanty Hall, Trinity Campus, 180 Colchester Avenue, Burlington, Vermont 05405, USA
[4]GNS Science, Dunedin Research Centre, 764 Cumberland Road, Private Bag 1930, Dunedin 9054, New Zealand
[5]Department of Earth Science, 1006 Webb Hall, University of California Santa Barbara, Santa Barbara, California 93106, USA
[6]School of Earth, Energy and Environmental Sciences, Stanford University, 397 Panama Mall, Mitchell Building 101, Stanford, California 94305, USA

ABSTRACT

The exhumed Fiordland sector of Zealandia offers a deep-crustal view into the life cycle of a Cordilleran-type orogen from final magmatic construction to extensional orogenic collapse. We integrate U-Pb thermochronologic data from metamorphic zircon and titanite with structural observations from >2000 km² of central Fiordland to document the tempo and thermal evolution of the lower crust during the tectonic transition from arc construction and crustal thickening to crustal thinning and extensional collapse. Data reveal that garnet granulite facies metamorphism and partial melting in the lower crust partially overlapped with crustal thickening and batholith construction during emplacement of the Western Fiordland Orthogneiss (WFO) from 118 to 115 Ma. Metamorphic zircons in metasedimentary rocks yield $^{206}Pb/^{238}U$ (sensitive high-resolution ion microprobe–reverse geometry) dates of 116.3–112.0 Ma. Titanite laser ablation split stream inductively coupled plasma–mass spectrometry chronology from the same rocks yielded complex results, with relict Paleozoic $^{206}Pb/^{238}U$ dates preserved at the margins of the WFO. Within extensional shear zones that developed in the thermal aureole of the WFO, titanite dates range from 116.2 to 107.6 Ma and have zirconium-in-titanite temperatures of ~900–750 °C. A minor population of metamorphic zircon rims and titanites in the Doubtful Sound region yield younger dates of 105.6–102.3 Ma with corresponding temperatures of 740–730 °C. Many samples record Cretaceous overdispersed dates with 5–10 m.y. ranges. Core-rim traverses and grain maps show complex chemical and temporal variations that cannot easily be attributed to thermally activated volume diffusion or simple core-rim crystallization. We interpret these Cretaceous titanites not as cooling ages, but rather as recording protracted growth and/or crystallization or recrystallization in response to fluid flow, deformation, and/or metamorphic reactions during the transition from garnet granulite to upper amphibolite facies metamorphism.

We propose a thermotectonic model that integrates our results with structural observations. Our data reveal a clear tectonic break at 108–106 Ma that marks a change in processes deep within the arc. Prior to this break, arc construction processes dominated and involved (1) emplacement of mafic to intermediate magmas of the Malaspina and Misty plutons from 118 to 115 Ma, (2) contractional deformation at the roof of the Misty pluton in the Caswell Sound fold-thrust belt from 117 to 113 Ma, and (3) eclogite to garnet granulite facies metamorphism and partial melting over >8 m.y. from 116 to 108 Ma. These processes were accompanied by complex patterns of lower crustal flow involving both horizontal and vertical displacements. After this interval, extensional orogenic collapse initiated along upper amphibolite facies shear zones in the Doubtful Sound shear zone at 108–106 Ma. Zircon and titanite growth and/or crystallization or recrystallization at this time clearly link upper amphibolite facies metamorphism to mylonitic fabrics in shear zones. Our observations are significant in that they reveal the persistence of a hot and weak lower crust for ≥15 m.y. following arc magmatism in central Fiordland. We propose that the existence of a thermally weakened lower crust within the Median Batholith was a key factor in controlling the transition from crustal thickening to crustal thinning and extensional orogenic collapse of the Zealandia Cordillera.

INTRODUCTION

Extensional collapse of Cordilleran-type orogenic belts is one of the primary driving mechanisms behind the fragmentation of convergent margins and the creation of microcontinents and continents (e.g., Zealandia; Mortimer, 2004; Rey and Müller, 2010). Processes that control extensional orogenic collapse commonly involve a decrease in frictional and viscous stresses due to changes in plate motions and/or arc root foundering, leading to the development of horizontal extension as buoyancy and gravitational stresses become increasingly important (Dewey, 1988; Rey et al., 2001, 2009; Rey and Müller, 2010). Styles of extensional faulting during orogenic collapse depend strongly on rheological contrasts between the upper and lower crust, and these rheological variations have a primary control on how and where strain is localized, including the development of detachment faults and gneiss domes (Buck, 1991; Lavier et al., 2000; Whitney et al., 2004; Huismans et al., 2005; Rey et al., 2009; Platt et al., 2014).

Numerical models that simulate rifting and extensional collapse commonly emphasize vertical rheological contrasts and thermal variations within

the crust as the principal controls on the styles of extensional faulting (e.g., Behn et al., 2002; Wijns et al., 2005; Lavier and Manatschal, 2006). In active Cordilleran-type orogens that are characterized by episodic deformation (contraction and extension) and magmatism and metamorphic pulses, the thermal and rheological structure of the crust changes as a function of magma flux rate, magma emplacement depth, and cooling rate (Hopper and Buck, 1998; Vanderhaeghe and Teyssier, 2001; Rey et al., 2001, 2009). Thus, styles of faulting in collapsing Cordilleran-type orogens are temporally linked to the evolving thermal and rheological structure of the crust, particularly the lower crust where magmatic activity is abundant, and heat flow and thermal weakening processes are dominant.

The concept of a thermally and rheologically evolving lower crust raises a number of questions regarding how strain is linked to the thermal structure of the crust and how it is accommodated during the collapse of orogenic belts. For example, over what time scales do thermal perturbations, including partial melting and high-temperature metamorphism, persist in the roots of orogens? How does the thermal structure of the lower crust change during ductile faulting and crustal thinning? What are the spatial dimensions of thermal perturbations and how long do they last? To what degree do mineral chronometers record passage through a closure temperature versus growth and/or crystallization or recrystallization in response to fluid flow, deformation and/or metamorphic reactions? How and where is strain focused during progressive metamorphism and cooling of the lower crust during extensional orogenic collapse?

To address these questions, we use titanite and zircon chronology and thermometry to investigate time scales and rates of metamorphism and the thermal structure of lower arc crust during collapse of the Fiordland sector of the Gondwana margin in the Cretaceous (Figs. 1 and 2). Here we use extensional orogenic collapse to refer to the tectonic transition from crustal thickening to crustal thinning and extension that eventually led to the rifting of Zealandia from Gondwana. Fiordland is unique among exposures of extended Zealandia (e.g., Mortimer, 2004) in that it preserves >5000 km^2 of lower crust that underwent granulite facies metamorphism and extensional collapse immediately following a high-flux magmatic event. Extensional faults related to orogenic collapse are not typically preserved in extended orogens (e.g., Kapp et al., 2008); however, in Fiordland, lower crustal extension was accommodated along a series of well-preserved, anastomosing low-angle shear zones that record an evolution of fabric development from disorganized shearing at eclogite and garnet granulite facies conditions to organized shearing at upper amphibolite facies conditions (Klepeis et al., 2007). Two of the most significant lower crustal extensional shear zones include the Doubtful Sound and Resolution Island shear zones, which consist of gently dipping zones of amphibolite facies mylonites that accommodated subhorizontal flow associated with crustal thinning, decompression, and cooling (Klepeis et al., 2007, 2016; Klepeis and King, 2009).

Despite a wealth of knowledge about the evolution of lower crustal structures in Fiordland, there is no consensus regarding when extensional orogenic collapse initiated and ceased, what structures accommodated extension in the deep crust, or the relationship between metamorphism and rheological transitions through time (e.g., Flowers et al., 2005; Klepeis et al., 2007; Stowell et al., 2014). The controversial thermotectonic history of Fiordland is illustrated in Figure 3, which shows two time-temperature models for the lower crust following the emplacement of the Western Fiordland Orthogneiss (WFO). In the Flowers et al. (2005) model (expanded upon by Klepeis et al., 2007), contractional thickening of the arc root resulted in granulite facies metamorphism and lower crustal flow, followed by rapid and short-lived (<6.2 m.y.), near isobaric cooling from 800 to 650 °C at ca. 116–111 Ma. Progressive localization of strain resulted in the formation of amphibolite facies mylonitic shear zones during a period of protracted cooling and exhumation of the arc root from 111 to 90 Ma (dashed line in Fig. 3). In contrast, in Stowell et al. (2014) it was proposed that the arc root remained above 800 °C from 116 to 111 Ma (solid line in Fig. 3), during the interval in which Flowers et al. (2005) proposed rapid cooling below 650 °C. In the Stowell et al. (2014) model, granulite facies metamorphism and partial melting persisted through the onset of lower crustal flow and extension at 111 Ma.

Here we use new thermochronologic data from lower crustal rocks sampled above, below, and within extensional faults to achieve the following specific goals: (1) determine the age and durations of lower crustal heating and cooling with the aim of resolving conflicting time-temperature paths; (2) evaluate the thermal structure of the Cretaceous arc root (40–65 km paleodepth) and how it has changed over >30 m.y. from 124 to 90 Ma; (3) link the thermal structure to tectonic transitions involving crustal thickening and crustal thinning; and (4) evaluate the timing of extensional orogenic collapse in the deep crust of Fiordland to middle and upper crustal extensional shear zones in greater Zealandia.

GEOLOGIC SETTING AND PREVIOUS WORK

Median Batholith and Prebatholithic Host Rocks in Central Fiordland

The South Island of New Zealand preserves a nearly complete exhumed section of a Mesozoic Cordilleran-type magmatic arc that was active along the paleo-Pacific margin of Gondwana prior to extensional orogenic collapse (Fig. 1) (Kimbrough et al., 1993, 1994; Mortimer et al., 1999; Hollis et al., 2004; Allibone et al., 2009a; Tulloch and Kimbrough, 2003). Arc-related plutonic and metaplutonic rocks collectively compose the ~10,000 km^2 composite Median Batholith (Mortimer et al., 1999), which was emplaced episodically over a period of ~250 m.y. from the Devonian to Early Cretaceous. In central Fiordland, the Mesozoic portion of the western Median Batholith is composed of variably metamorphosed Early Cretaceous diorite, monzodiorite, and minor gabbro of the WFO, a major component of the high Sr/Y Separation Point Suite (Bradshaw, 1989b; Allibone et al., 2009a; De Paoli et al., 2009). Major plutons of the WFO include the Worsley, Misty, and Malaspina plutons as well as the Breaksea and Resolution Orthogneisses (Fig. 2). The WFO was emplaced during a short-lived, high-flux magmatic event from ca. 125 to 115 Ma (Mattinson et al., 1986; Tulloch and Kimbrough, 2003; Hollis et al., 2003, 2004; Bolhar et al., 2008; Sadorski, 2015). Batholith construction in central Fiordland was

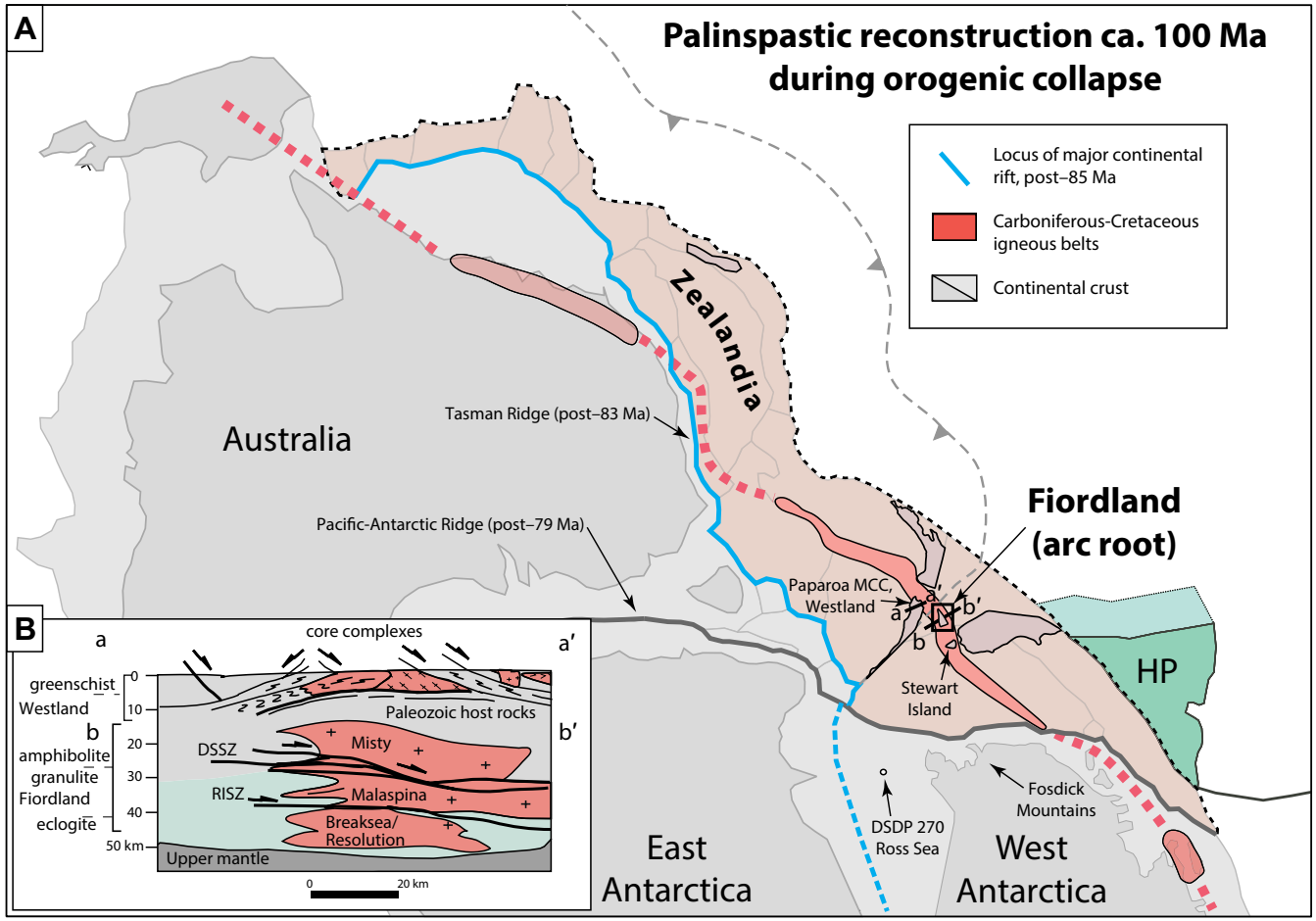

Figure 1. (A) Palinspastic reconstruction of the Gondwana margin and Zealandia ca. 100 Ma during extensional orogenic collapse (modified after Mortimer, 2008). Westland, Stewart Island, and Fiordland typify parts of the shallow to deep crustal components of the Cordilleran-type Gondwanan arc (red shaded belt) prior to orogenic collapse. (B) Inset shows schematic reconstruction of Westland (upper to middle crust) and Fiordland (middle to lower crust) during extensional orogenic collapse (after Klepeis et al., 2003). HP—Hikurangi Plateau (green shaded region in A); DSSZ—Doubtful Sound shear zone; RISZ—Resolution Island shear zone; DSDP—Deep Sea Drilling Project; MCC—metamorphic core complex.

synchronous with contractional deformation in northern Fiordland (Pembroke Valley and Mount Daniel) and in the Caswell Sound fold-thrust belt (Daczko et al., 2001, 2002; Klepeis et al., 2004).

Prebatholithic host rocks to the WFO consist of variably metamorphosed and deformed meta-igneous and metasedimentary rocks of the early Paleozoic Takaka terrane. Metasedimentary rocks are collectively termed the Deep Cove Gneiss and chiefly consist of quartzofeldspathic paragneiss, marble, calc-silicate, and hornblende-plagioclase gneiss (Oliver, 1980; Gibson, 1992). Based on correlations with lower grade metasedimentary rocks in Westland (Fig. 1), northwest South Island (Cooper and Tulloch, 1992), the depositional ages for the metasedimentary rocks in this sequence are believed to range from Middle Cambrian to Silurian; however, little age control exists in Fiordland due to multiple pulses of high-temperature metamorphism. Pre-Cretaceous meta-igneous rocks consist of Late Devonian–late Carboniferous I-type and S-type granitic rocks ranging from 371 to 305 Ma (Tulloch et al., 2009a), and minor Ordovician orthogneiss (Gibson and Ireland, 1996).

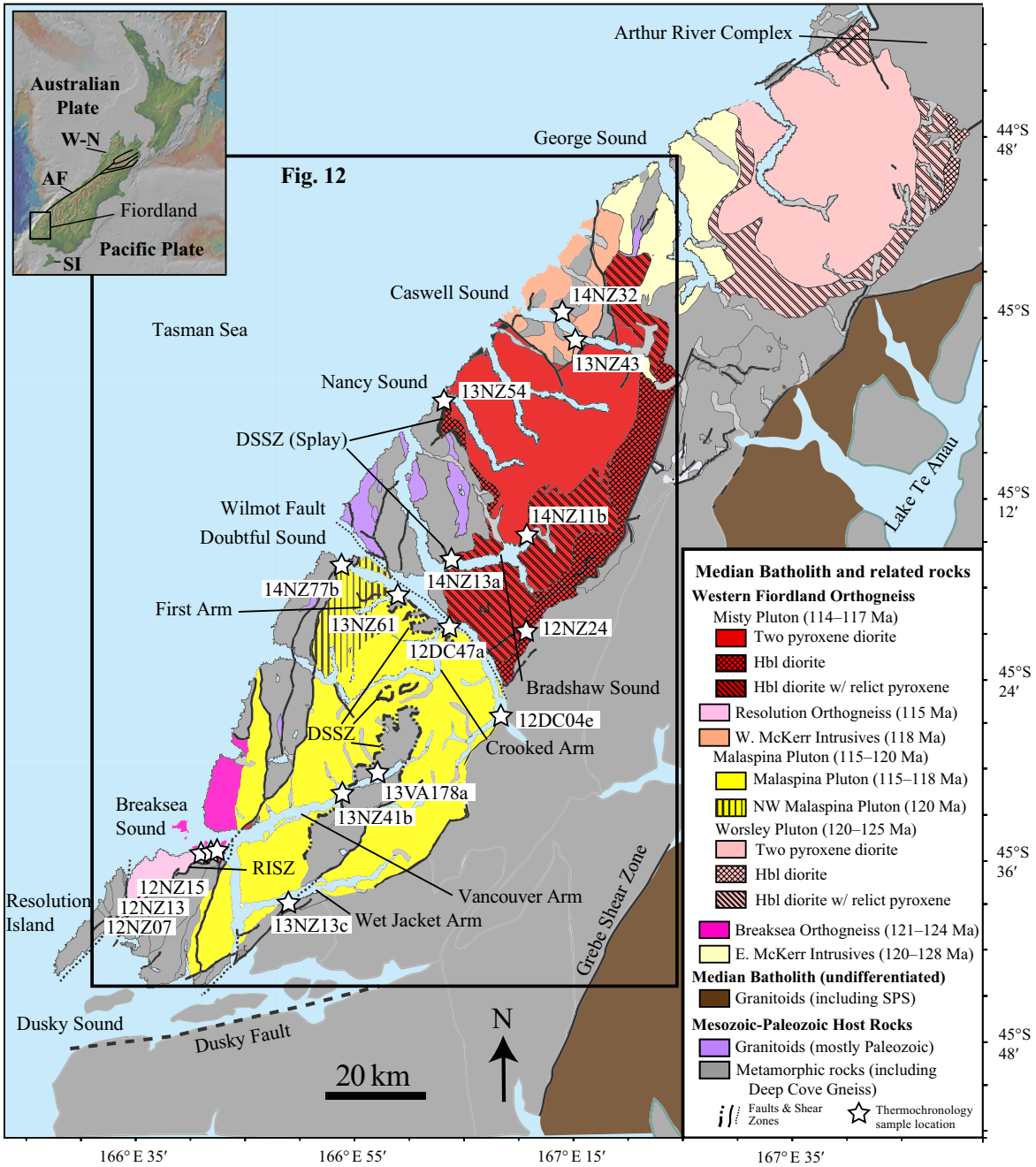

Figure 2. Geologic map of central Fiordland, New Zealand, focusing on the Western Fiordland Orthogneiss (WFO) and surrounding prebatholithic rocks (after Allibone et al., 2009a; Sadorski, 2015). Sample locations shown by white star. DSSZ—Doubtful Sound shear zone; RISZ—Resolution Island shear zone. Inset shows location of Fiordland in New Zealand. W-N—Westland-Nelson region; AF—Alpine fault; SI—Stewart Island; hbl—hornblende; SPS—Separation Point Suite.

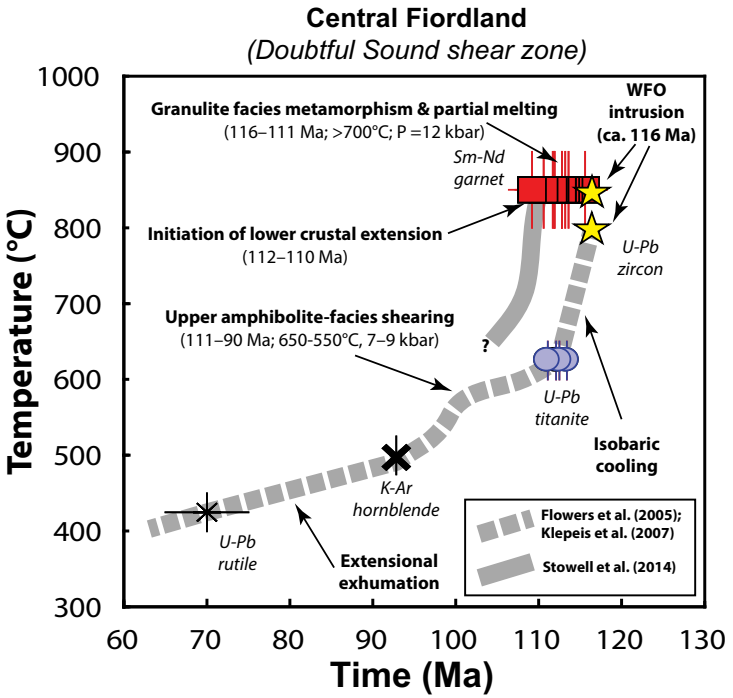

Figure 3. Time-temperature plot for central Fiordland showing competing and conflicting thermal models for the evolution of the lower crust following Western Fiordland Orthogneiss (WFO) emplacement. In the Flowers et al. (2005) and Klepeis et al. (2007) model, the lower crust cools rapidly and isobarically in <6.2 m.y. Decompression and extension occur from 111 to 90 Ma. In contrast, the Stowell et al. (2014) model shows the lower crust remaining hot (>700 °C) and weak through 110 Ma with no evidence for rapid isobaric cooling during this interval.

Lower Crustal Extensional Structures and Fabric Evolution

Most contacts between the WFO and prebatholithic host rocks are characterized by thin, 10–100 m bands of upper amphibolite facies mylonites that form branching networks of high-strain extensional shear zones (Gibson et al., 1988; Klepeis et al., 2007, 2016). Mylonitic marbles and associated paragneisses are commonly located in the hanging wall of high-strain shear zones and mark the boundary between the WFO and prebatholithic rocks. Regional mapping in central Fiordland has led to the recognition of two principal extensional shear zones, the Doubtful Sound and Resolution Island shear zones (Fig. 2) (Klepeis et al., 2007, 2016; Allibone et al., 2009a, 2009b). The Doubtful Sound shear zone has received significant attention in the literature as a possible large-magnitude, lower crustal detachment fault (e.g., Gibson et al., 1988; Oliver, 1990); however, this interpretation is controversial. Gibson and Ireland (1995) argued that ~9–12 km of middle crust were removed during Early Cretaceous extension, based on 2.5–3 kbar differences in metamorphic pressure between the footwall WFO (10–12 kbar) and hanging-wall Deep Cove Gneiss (7–9 kbar). However, Allibone et al. (2009b) noted that the estimates of large-magnitude displacements are based on contrasting mineral assemblages that may have formed at different times; they argued for smaller displacements based on regional mapping and thermobarometry of preserved intrusive contacts between WFO and prebatholithic host rocks. Allibone et al. (2009b) concluded that the WFO intruded the Deep Cove Gneiss at high pressures and that recrystallization of adjacent Deep Cove Gneiss occurred within a 200–1000 m (present thickness) garnet granulite facies thermal aureole of the WFO (also see Daczko et al., 2009).

Timing of Metamorphism and Extensional Orogenic Collapse

Existing geochronology of metamorphic rocks in central Fiordland documents three episodes of Paleozoic to Cretaceous high-grade metamorphism: (1) a low-*P*–high-*T* event at 375–355 Ma, (2) a medium-*P*–high-*T* event at 340–315 Ma, and (3) a high-*P*–high-*T* event from ca. 125 to 110 Ma (Ireland and Gibson, 1998; Klepeis et al., 1999, 2004, 2007; Clarke et al., 2000; Chavez et al., 2007; Daczko et al., 2009; Stowell et al., 2010, 2014; De Paoli et al., 2009). The former two events record deformation and metamorphism along the paleo-Pacific margin of Gondwana and have been linked to events in the Lachlan Fold Belt in southeast Australia (Gibson, 1992; Foster and Gray, 2000). The last phase of metamorphism resulted in localized migmatization of prebatholitic host rocks in the contact aureole of the WFO and localized partial melting of the WFO (Oliver, 1980; Gibson and Ireland, 1995; Allibone et al., 2009b; Daczko et al., 2009). Peak Cretaceous metamorphic conditions recorded in central Fiordland range from 10 to 18 kbar and 800 to 920 °C (Gibson and Ireland, 1995; Hollis et al., 2004; Klepeis et al., 2007; De Paoli et al., 2009; Stowell et al., 2014).

Lower crustal flow within central Fiordland is recorded by early crystal-plastic deformation of prograde garnet granulite facies mineral assemblages (Klepeis et al., 2007, 2016; Betka and Klepeis, 2013). Nine garnet Sm-Nd dates from partially melted granulites and a garnet pyroxenite interpreted to record the timing of high-grade metamorphism from 115.6 ± 2.2 to 110.6 ± 2.0 Ma (2σ) were reported in Stowell et al. (2014). One crystal-plastically deformed clinopyroxene-garnet assemblage yielded an age of 112.8 ± 2.2 Ma (2σ) at conditions of 14–15 kbar and ~920 °C, indicating that lower crustal flow was underway shortly after WFO emplacement (Stowell et al., 2014). Trondhjemitic veins and garnet reaction zones locally cut early garnet granulite facies foliations. One trondhjemitic leucosome vein gave a U-Pb sensitive high-resolution ion microprobe (SHRIMP) zircon date of 114.2 ± 2.2 Ma (2σ; Hollis et al., 2004).

Evidence for a hot lower crust that persisted for >5 m.y. at granulite facies conditions following WFO emplacement conflicts with single and multigrain titanite thermal ionization mass spectrometry dates of 113.4 ± 0.4 Ma to 111.1 ± 0.5 Ma (2σ) that were interpreted by Flowers et al. (2005) to document rapid lower crustal cooling from ~850–650 °C in ≤6.2 m.y. without significant exhumation (Fig. 3). The interpretation of rapid cooling of the arc root was

based on the assumption that the titanite dates record thermally activated volume diffusion, a conclusion that we dispute. Based in part on these titanite dates, Klepeis et al. (2007) proposed that exhumation and extension at upper amphibolite facies conditions along the Doubtful Sound shear zone occurred from 111 to 90 Ma. These dates also conflict with a zircon ion probe date of 119 ± 5 Ma (1σ) from an amphibolite in the same shear zone that Gibson et al. (1988) interpreted as representing the timing of extension. A K-Ar hornblende date of 92.6 ± 1.8 Ma (2σ) was used Gibson et al. (1988) to document cooling of the footwall to the Doubtful Sound shear zone through ~500–550 °C. By ca. 83 Ma, Zealandia rifted from the proto-Gondwana margin and seafloor spreading had initiated in the Tasman Sea (Gaina et al., 1998; Tulloch et al., 2009b).

METHODS

Sampling Strategy

Our helicopter and boat sampling covers >2000 km² and consists of 15 zircon- and titanite-bearing metasedimentary and metaigneous rocks collected structurally above, below, and within extensional shear zones including the Doubtful Sound shear zone (DSSZ) and the Resolution Island shear zone (RISZ) (Table 1). Shear zone, hanging-wall, and footwall samples consist of 12 calc-silicates, paragneisses, and amphibolites of the Deep Cove Gneiss (Takaka terrane) and 2 samples from the WFO (Misty pluton and Resolution Orthogneiss). Shear zone samples include two samples from within the RISZ (12NZ12, 12NZ15), eight samples within the DSSZ (13NZ41b, 12DC04e, 12DC47a, 13NZ61, 14NZ77b), and two samples within splays of the DSSZ at the entrance to Bradshaw Sound (14NZ13a) and Nancy Sound (13NZ54). Hanging-wall samples include three samples from above the DSSZ (13VA178a, 12NZ24, and 14NZ11b). Footwall samples include a garnet granulite orthogneiss from the Resolution Orthogneiss located below the RISZ (12NZ07), and a calc-silicate below the projection of the DSSZ at Wet Jacket arm (13NZ13c). One paragneiss was also collected from within a ductile shear zone in the Caswell Sound fold-thrust belt (13NZ43). A postkinematic dike (14NZ32) from the same area was also collected to constrain the timing of contractional deformation. (For additional details regarding samples, see Figs. 4 and 5, Table 1, and the Results discussion.)

Zircon and Titanite Chronology and Geochemistry

Zircon and titanite were separated following standard methods involving density (Wilfley table and heavy liquids) and magnetic (Frantz isodynamic separator) separation techniques at California State University Northridge. Zircons and titanite were mounted in epoxy, ground and polished, and imaged on a FEI Quanta 600 variable pressure environmental scanning electron microscope (SEM). Zircons were imaged in cathodoluminescence (CL) using a Gatan MiniCL detector, and titanite were imaged on a backscattered (BSE) electron detector. Zircon U-Pb geochronology and trace element analyses (Y, rare earth elements, Hf) were conducted simultaneously using an average spot size of ~22–28 μm at the U.S. Geological Survey–Stanford SHRIMP-RG (reverse geometry) facility (see text in Supplemental File[1] for analytical details). Reported zircon dates are the common Pb-corrected $^{206}Pb/^{238}U$ dates.

SUPPLEMENTAL FILE

LIST OF FILES INCLUDED IN SUPPLEMENTAL FILE

Supplemental Text: Detailed description of methods.

Supplemental Table 1: Sample locations and descriptions.

Supplemental Table 2: U-Pb zircon SHRIMP-RG isotopic data and ages.

Supplemental Table 3: U-Pb titanite LA-MC-ICP-MS isotopic data and ages.

Supplemental Table 4: Titanite LA-Q-ICP-MS geochemical data.

Supplemental Table 5: Zircon trace element geochemical data.

[1]Supplemental File. Detailed description of methods and five tables. Please visit http://dx.doi.org/10.1130/GES01232.S1 or the full-text article on www.gsapubs.org to view the Supplemental File.

TABLE 1. SAMPLE LOCALITIES AND PETROGRAPHY

Sample	Lithology	Structure	Location	Assemblage	Deformation and/or Textural Features
12NZ07	Garnet orthogneiss	RISZ (footwall)	Breaksea Sound	Grt-Pl-Hbl-Di-Ilm-Rt-Ap-Ttn	Weak S_2; Grt inclusion in Hbl; Ilm and Rt inclusion in Ttn; Hbl-Pl-Di symplectites.
12NZ13	Calc-silicate gneiss	RISZ (shear zone)	Breaksea Sound	Cal-Di-Grt-Pl-Qz-Ttn-Zrc-Ap	Weak S_3; Cal locally granoblastic and kinked; Ttn to 1 mm weakly aligned with S_3.
12NZ15	Calc-silicate gneiss	RISZ (shear zone)	Breaksea Sound	Cal-Di-Grt-Pl-Qz-Ttn-Zrc-Ap-Scp	Strong S_3; Cal recrystallized and kinked.
13NZ13c	Calc-silicate gneiss	DSSZ (footwall)	Wet Jacket Sound	Cal-Di-Grt-Pl-Qz-Ttn-Zrc-Ap	Fine-grained, mylonitic S_3 fabric.
12DC04e	Paragneiss	DSSZ (shear zone)	Hall Arm	Hbl-Pl-Qz-Di-Ep-Ttn-Zrc-Ap	Strong S_3 foliation with Ttn aligned in fabric.
13NZ61	Paragneiss	DSSZ (shear zone)	First Arm	Di-Hbl-Pl-Kfs-Ap-Zrc-Ttn-Mag	Strong S_3 with tight isoclinal folds.
14NZ77b	Amphibolite	DSSZ (shear zone)	Cascadia Bay	Hbl-Pl-Di-Ttn-Ep	Ttn aligned in moderate to strong S_3 fabric; late Ep veins cut fabric.
13NZ54	Calc-silicate gneiss	DSSZ (shear zone)	Nancy Sound	Cal-Di-Hbl-Bt-Pl-Qz-Ttn-Zrc-Ap	Strong S_3 foliation; Ttn aligned in fine-grained Cal.
12DC47a	Calc-silicate gneiss	DSSZ (shear zone)	Kellard Point	Cal-Di-Grt-Pl-Qz-Ttn-Zrc-Ap-Scp	Strong S_3; Cal recrystallized and kinked; Ttn aligned with S_3.
13NZ41b	Calc-silicate gneiss	DSSZ (shear zone)	Vancouver Arm	Cal-Di-Bt-Pl-Qz-Ttn-Zrc-Ap	Strong S_3; Cal recrystallized and kinked; Ttn aligned with S_3.
14NZ13a	Calc-silicate gneiss	DSSZ (shear zone)	Bradshaw Sound	Cal-Di-Qz-Scp-Ttn-Zrc-Ap	Strong S_3 mylonitic fabric.
12NZ24	Hornblende diorite	DSSZ (hanging wall)	Marington Peaks	Pl-Hbl-Bt-Ep-Czo-Ilm-Mag	No evidence for crystal-plastic deformation.
14NZ11b	Calc-silicate gneiss	DSSZ (hanging wall)	Bradshaw Sound	Cal-Di-Scp-Pl-Qz-Ttn-Zrc-Ap	S-C mylonite with strong S_3 fabric.
13VA178a	Calc-silicate gneiss	DSSZ (hanging wall)	Vancouver Arm	Cal-Di-Pl-Qz-Bt-Ttn-Zrc-Ap	Weak S_3 fabric; Ttn randomly aligned in fabric.
13NZ43	Paragneiss	CS ftb (shear zone)	Caswell Sound	Di-Hbl-Pl-Ca-Qz-Ep-Ap-Zrc-Ttn	Moderately foliated with granoblastic overprint.
14NZ32	Granitic dike	CS ftb (shear zone)	Caswell Sound	Pl-Kfs-Bt-Ms-Qz-Czo-Zrc	Postkinematic dike, cuts mylonitic fabric in host Caswell gneiss.

Note: RISZ—Resolution Island shear zone; DSSZ—Doubtful Sound shear zone; CS ftb—Caswell Sound fold-thrust belt. Mineral abbreviations are after Whitney and Evans (2010): Grt—garnet; Pl—plagioclase; Hbl—hornblende; Di—diopside; Ilm—ilmenite; Rt—rutile; Ap—apatite; Ttn—titanite; Cal—calcite; Qz—quartz; Zrn—zircon; Scp—scapolite; Bt—biotite; Ep—epidote; Czo—clinozoisite; Kfs—K-feldspar; Mag—magnetite; Ms—muscovite.

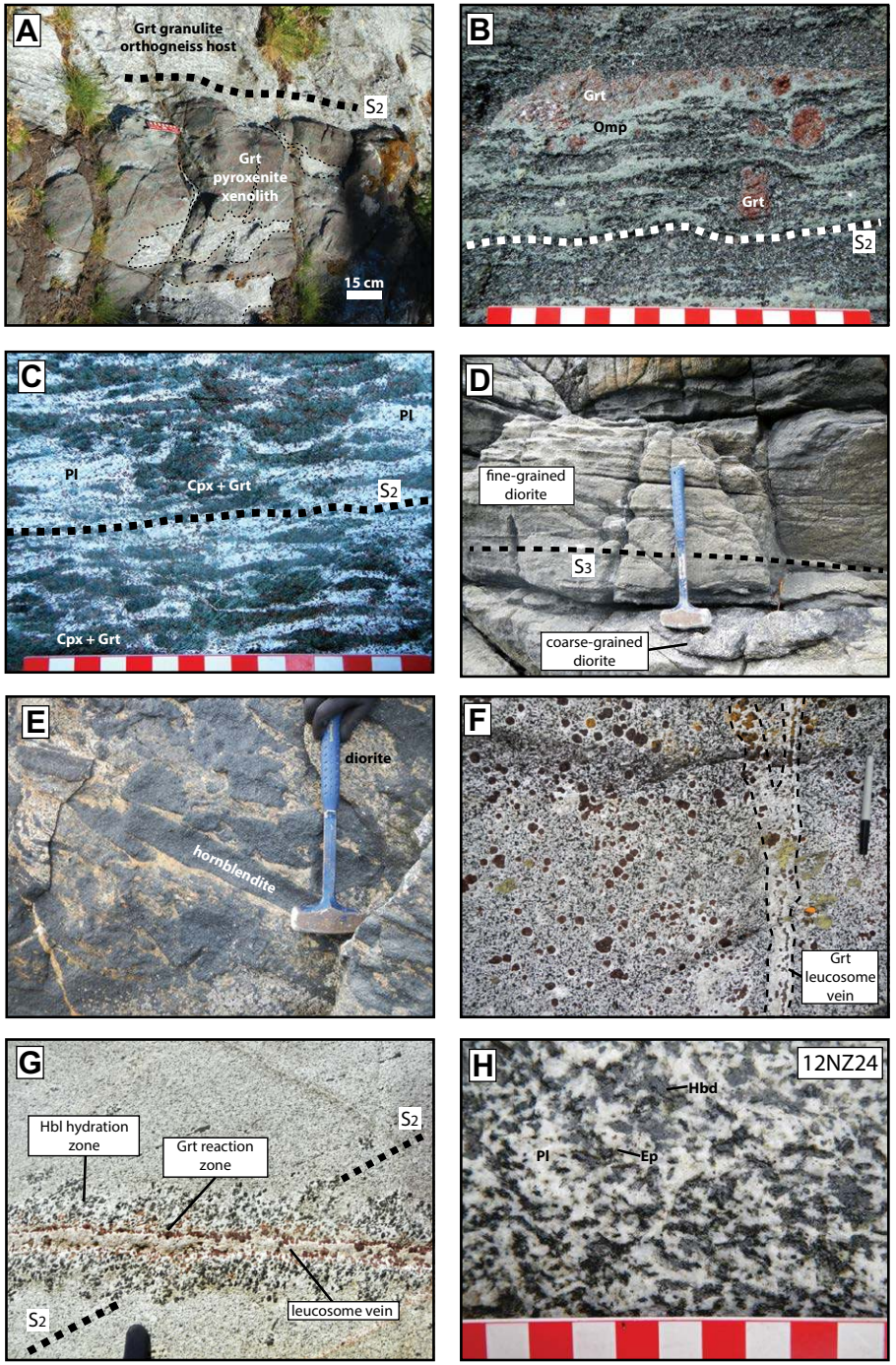

Figure 4. Field photos illustrating structures developed in central Fiordland. (A) Intrusion of granulitic orthogneiss into xenoliths of garnet pyroxenite in the Breaksea Orthogneiss. The granulite is migmatitic and displays a well-developed S_2 foliation. (B) Garnet (Grt) pyroxenite in the Breaksea Orthogneiss showing internal S_2 foliation that disrupts original cumulate layering (Omp—omphacite). (C) Migmatitic garnet graunulite host (Breaksea Orthogneiss) with well-developed S_2 foliation. Fine-grained garnet is developed throughout a plagioclase (Pl) rich matrix. Lenses and layers of omphacite are retrogressed locally to hornblende (Cpx—clinopyroxene). (D) Relict igneous layering of fine- and coarse-grained diorite is transposed into tight S_3 axial planar foliation in the footwall to the Resolution Island shear zone. (E) Angular brecciated fragments of hornblendite in host diorite (Misty pluton, Nancy Sound) formed during Western Fiordland Orthogneiss emplacement. (F) Disseminated garnet in a low-strain migmatitic diorite (Misty pluton) with garnet-bearing leucosome. Large (1 cm) garnets have plagioclase halos. (G) Granodioritic leucosome vein with garnet reaction zone intruding diorite (Misty pluton). Leucosome cuts S_2 foliation defined by aligned clots of clinopyroxene. A hornblende (Hbl) reaction zone is developed within 2–3 cm around the leucosome, suggesting hydration of the host during vein emplacement. (H) Hornblende diorite (Misty pluton) located in the hanging wall of the Doubtful Sound shear zone. Sample 12NZ24 lacks foliation but has strong amphibolite facies overprint defined by development of green hornblende, epidote (Ep), clinozoisite, and titanite. Red and white boxes on scale bar are 1 cm in length.

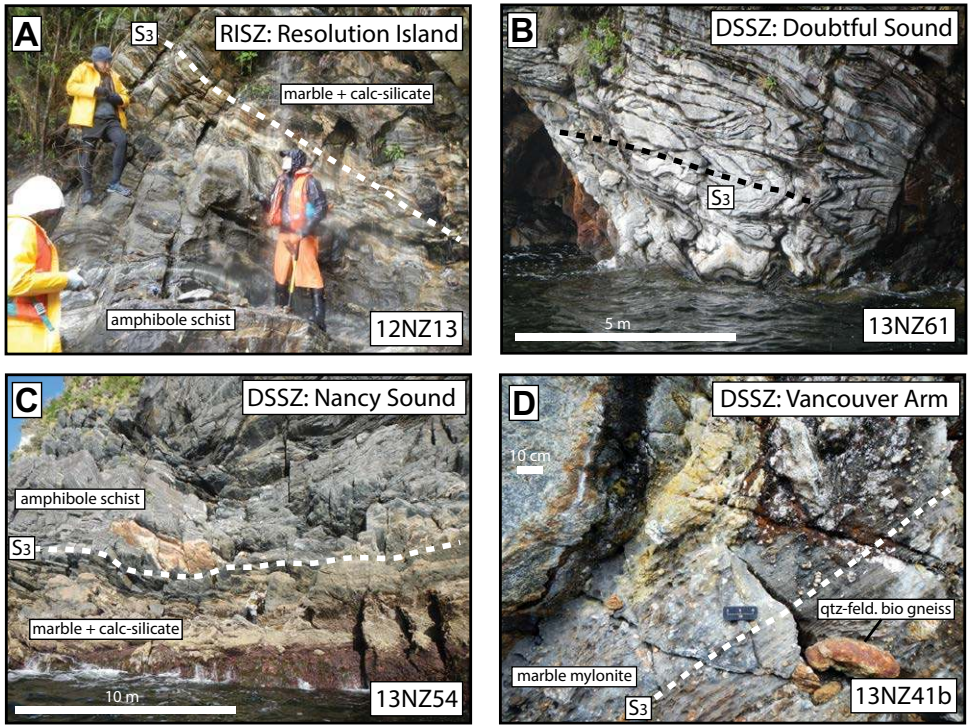

Figure 5. Field photos illustrating structures developed in extensional shear zones in central Fiordland. (A) Shallow to moderately dipping calc-silicates and amphibole schist in Resolution Island shear zone (RISZ). (B) Isoclinal folding of Deep Cove Gneiss during shearing in Doubtful Sound (DSSZ—Doubtful Sound shear zone). (C) High-strain zone at the entrance to Nancy Sound where a splay of the DSSZ shows strong S_3 foliation developed in amphibolites, marble, and calc-silicates (Deep Cove Gneiss). (D) High-strain zone in the DSSZ (Vancouver Arm) showing clasts of quartzofeldspathic biotite (qtz-feld. bio) gneiss enveloped within a mylonitic marble host.

Zircon trace element data were collected from zircon-bearing calc-silicates and paragneisses to verify that zircons within extensional shear zones represent new metamorphic growth and not igneous xenocrysts derived from tectonic shearing of the adjacent WFO. Results are compared to those of the WFO from Sadorski (2015).

Titanite chronology and geochemistry were performed at the University of Santa Barbara laser ablation split stream inductively coupled plasma–mass spectrometry (LASS, ICP-MS) laboratory following methods outlined in Kylander-Clark et al. (2013) and Spencer et al. (2013). Titanite ages for samples are presented as lower intercepts calculated from regression of $^{207}Pb/^{206}Pb$–$^{238}U/^{206}Pb$ data using Isoplot 3.75 (Ludwig, 2012). In a few cases where titanites display limited spread in $^{207}Pb/^{206}Pb$–$^{238}U/^{206}Pb$, a fixed $^{207}Pb/^{206}Pb$ value of 0.83 is used to calculate dates. When discussing individual dates, we refer to common Pb-corrected $^{206}Pb/^{238}U$ dates whereby common Pb values are based on either y-intercepts of regressed $^{207}Pb/^{206}Pb$–$^{238}U/^{206}Pb$ data or an assumed value of 0.83. The quoted dates in the text and tables are assigned 2% absolute uncertainties based on reproducibility of standards during analyses, except when comparing analyses within the same sample or grain; in the latter case, uncertainties are reported as 2σ standard error of internal measurements only. Detailed descriptions of the methods for isotopic analysis and sample locations are provided in the Supplemental File text. Zircon and titanite data are also reported in the Supplemental File text, and summarized in Tables 2 and 3. Geochronologic and geochemical data are presented in Figures 6–11.

Titanite Thermometry

We use LASS Zr measurements of titanite and the Hayden et al. (2008) calibration to assess titanite crystallization or recrystallization temperatures. Analytical uncertainties on Zr measurements range from 5% to 10% (2 standard error, SE) resulting in temperature uncertainties of 5–10 °C (Supplemental File text, Supplemental Table 4). Incorporation of pressure and activity uncertainties results in larger temperature uncertainties. For example, all samples contain quartz and zircon (except two mafic orthogneisses, 12NZ07 and 14NZ77b), fixing the $aSiO_2$ and $aZrSiO_4$ at unity for most samples. Note that samples 12NZ07 and 14NZ77b yield dates with large uncertainties and consequently their dates and temperatures are not emphasized in this study. The activity of TiO_2 is assumed to be unity; however, this is a maximum because most

TABLE 2. SUMMARY OF METAMORPHIC ZIRCON AND TITANITE DATES AND TEMPERATURES IN WESTERN FIORDLAND, NEW ZEALAND

Sample	Titanite* type	Titanite† ages	Error (2σ)	MSWD	Titanite§ temperatures	Standard deviation (1σ)	Zircon** ages	Error (2σ)	MSWD	Number (spots)
13VA178a	P	330.1	6.6	n.a.	754	19	n.d.	n.d.	n.d.	n.d.
		104.9	7.4	0.0	699	1				
12DC04e	P	110.1	4.5	11.6	829	20	n.d.	n.d.	n.d.	n.d.
13NZ43	C	113.6	2.3	1.0	853	18	n.d.	n.d.	n.d.	n.d.
13NZ61	C	111.2	2.2	0.6	767	13	116.3	1.7	2.2	8
							105.6	1.9	1.2	7
12NZ13	C	110.5	2.2	1.0	841	22	112.0	1.4	1.5	11
12NZ15	C	110.4	2.2	3.2	896	28	113.9	2.0	1.5	9
12NZ24	C	104.7	4.1	0.2	742	22	115.8	1.9	1.5	8
14NZ77b	C	99.0	13.0	0.7	770	21	n.d.	n.d.	n.d.	n.d.
12NZ07	C	95.2	8.9	2.2	816	16	n.d.	n.d.	n.d.	n.d.
13NZ54	O	116.2	2.3	4.3	860	32	114.7	1.6	2.3	10
		109.0	2.2	3.6	851	35	112.4	1.3	1.3	10
12DC47a	O	116.0	2.3	1.2	859	32	112.6	0.8	0.9	12
		110.0	2.2	2.8	n.d.	n.d.				
13NZ13c	O	115.3	2.3	1.6	887	14	n.d.	n.d.	n.d.	n.d.
		110.4	2.2	0.7	885	14				
14NZ11b	O	114.5	2.3	1.5	831	20	n.d.	n.d.	n.d.	n.d.
		109.4	2.2	0.9	790	27				
13NZ41b	O	111.4	2.2	1.1	777	9	n.d.	n.d.	n.d.	n.d.
		107.6	2.2	0.8	753	15				
14NZ13a	O	108.3	2.2	3.6	811	28	n.d.	n.d.	n.d.	n.d.
		102.3	2.0	2.4	728	17				

Note: MSWD—mean square of weighted deviates; n.d.—not determined; n.a.—not applicable.
*P—pre-Cretaceous dates; C—Cretaceous dates; O—overdispersed Cretaceous dates (see text).
†Ages determined by laser ablation–multicollector–inductively coupled plasma–mass spectrometry (LA-MC-ICP-MS). Reported ages are lower intercept ages defined by isochron regressions on Tera-Wasserburg concordia diagrams (see footnotes in Supplemental Table 3).
§Zirconium-in-titanite temperatures calculated from qLA-ICP-MS data except samples 12NZ15 and 12DC47a, determined by sensitive high-resolution ion microprobe–reverse geometry (SHRIMP-RG). Zirconium-in-titanite temperatures were calculated following Hayden et al. (2008), assuming pressure, P = 1.0 GPa, $a\mathrm{TiO_2}$ = 1.0, $a\mathrm{SiO_2}$ = 1.0, except 13VA178a, where P = 0.8 GPa.
**Error-weighted average ages determined by SHRIMP-RG.

samples lack rutile. For samples with ilmenite, $a\mathrm{TiO_2}$ is likely >0.8, resulting in an ~15 °C decrease in calculated temperature (Chambers and Kohn, 2012). Most calc-silicates lack rutile and ilmenite; however, because samples contain titanite, $a\mathrm{TiO_2}$ is constrained to at least 0.5 (Hayden et al., 2008). Assuming a lower estimate for $a\mathrm{TiO_2}$ of 0.5 results in a decrease in temperature of ~20 °C. Notably, in the original Hayden et al. (2008) experiments, a rutile-absent run with excess CaO resulted in average Zr concentrations that were statistically indistinct from rutile-saturated runs. Pressure estimates for granulite to amphibolite facies metamorphism in central Fiordland range from 1.5 to 0.7 GPa (Oliver, 1977; Bradshaw, 1989a, 1989b; Gibson and Ireland, 1995; Brown, 1996; Hollis et al., 2004; Klepeis et al., 2007; Stowell et al., 2014). Peak metamorphic pressure estimates below the RISZ are somewhat higher, ranging to 1.8 GPa; however, titanite is commonly developed in retrograde fabrics that record pressures ranging from 1.4 to 0.9 GPa at 115–88 Ma (De Paoli et al., 2009; Betka and Klepeis, 2013). We assume an intermediate pressure value of 1.0 GPa for all samples during metamorphism and extensional orogenic collapse. However, it is possible that titanite growth initiated at high-P conditions; a 0.4 GPa uncertainty in pressure results in an ~50 °C uncertainty in calculated temperature. Given these uncertainties in measurements, pressure, and activities, we conservatively apply an uncertainty of ±50 °C to all our temperature estimates.

Zircon and Titanite Pb Mobility and Closure Temperatures

Intracrystalline volume diffusion of Pb in zircon is typically considered to be a sluggish process resulting in closure temperatures in excess of 900 °C for a typical 100 μm zircon (assuming 10 °C/m.y. cooling rate; Cherniak and Watson, 2001).

TABLE 3. SUMMARY OF ZIRCON, GARNET AND TITANITE DATES AND TEMPERATURES FOR WESTERN FIORDLAND ORTHOGNEISS AND HOST ROCKS IN WESTERN FIORDLAND, NEW ZEALAND

Sample	Unit	Rock type	Long.* (dd)	Lat.* (dd)	Age (Ma)	Absolute error (Ma; 2σ)	Temperature† (°C)	Absolute error (°C; 2 standard deviation)	Reference material (primary)	Reference
Igneous zircon chronology§										
13NZ33E	Breaksea Orthogneiss	garnet orthogneiss	166.6424	–45.5922	123.2	1.3	n.d.	n.d.	R33	Klepeis et al. (2016)
13NZ59	Northwest Malaspina pluton	hornblende orthogneiss	166.9129	–45.3401	120.3	1.4	840	60	R33	Sadorski (2015)
13NZ34A	Malaspina pluton	garnet orthogneiss	166.7189	–45.6547	118.0	1.6	790	60	R33	Sadorski (2015)
13N16B	Malaspina pluton	garnet orthogneiss	166.7203	–45.6937	118.0	1.7	780	80	R33	Sadorski (2015)
12NZ17b	Malaspina pluton	garnet leucosome	166.7935	–45.5686	117.0	1.5	n.d.	n.d.	R33	Sadorski (2015)
13NZ46	Misty pluton	orthogneiss	167.2902	–45.0442	116.9	1.8	800	20	R33	Sadorski (2015)
13NZ22	Malaspina pluton	orthogneiss	166.7906	–45.5697	116.9	1.8	810	60	R33	Sadorski (2015)
13NZ52A	Misty pluton	orthogneiss	167.1568	–45.0925	116.8	2.1	830	30	R33	Sadorski (2015)
13NZ40D	Malaspina pluton	orthogneiss	166.8534	–45.5497	116.4	1.6	780	60	R33	Sadorski (2015)
OU49113	Malaspina pluton	orthogneiss	166.9535	–45.6192	116.3	n.d.	n.d.	n.d.	n.a.	Tulloch and Kimbrough (2003)
12NZ24	Misty pluton	orthogneiss	167.1720	–45.3449	115.8	1.7	n.d.	n.d.	R33	Sadorski (2015)
CA90	Malaspina pluton	orthogneiss	167.0303	–45.3969	115.6	2.4	n.d.	n.d.	Temora	Hollis et al. (2004)
12DC41	Malaspina pluton	orthogneiss	166.9366	–45.4137	115.4	1.8	n.d.	n.d.	R33	Sadorski (2015)
13NZ58	Misty pluton	orthogneiss	167.0909	–45.1556	115.3	2.0	740	60	R33	Sadorski (2015)
13NZ55A	Misty pluton	orthogneiss	167.0396	–45.1141	115.2	1.9	820	100	R33	Sadorski (2015)
12NZ22	Misty pluton	orthogneiss	167.1093	–45.3072	114.7	1.7	n.d.	n.d.	R33	Sadorski (2015)
12NZ33	Misty pluton	orthogneiss	167.1540	–45.3059	114.5	2.6	n.d.	n.d.	R33	Sadorski (2015)
12NZ36	Misty pluton	orthogneiss	167.1390	–45.2714	114.2	1.3	n.d.	n.d.	R33	Sadorski (2015)
Metamorphic zircon chronology										
CA39M	Takaka terrane	paragneiss	167.0453	–45.3546	120.8	2.3	n.d.	n.d.	Temora	Hollis et al. (2004)
13NZ04B	Takaka terrane	garnet orthogneiss	167.0502	–45.3781	117.2	0.8	n.d.	n.d.	R33	Klepeis et al. (2016)
13NZ61	Takaka terrane	paragneiss	166.9623	–45.3208	116.3	1.7	n.d.	n.d.	R33	Schwartz et al. (this study)
CA39M	Takaka terrane	paragneiss	167.0453	–45.3546	114.9	2.2	n.d.	n.d.	Temora	Hollis et al. (2004)
CA10	Malaspina pluton	garnet reaction zone	167.0198	–45.4110	114.0	2.2	n.d.	n.d.	Temora	Hollis et al. (2004)
12NZ15	Takaka terrane	calc-silicate	166.6868	–45.6043	113.9	1.6	n.d.	n.d.	R33	Schwartz et al. (this study)
12DC04E	Takaka terrane	paragneiss	167.1316	–45.4446	113.5	1.7	n.d.	n.d.	R33	Klepeis et al. (2016)
12DC47A	Takaka terrane	calc-silicate	167.0351	–45.3574	112.6	0.8	n.d.	n.d.	R33	Schwartz et al. (this study)
13NZ54	Takaka terrane	calc-silicate	167.0131	–45.1101	112.4	1.3	n.d.	n.d.	R33	Schwartz et al. (this study)
12NZ13	Takaka terrane	calc-silicate	166.6861	–45.6028	112.0	1.4	n.d.	n.d.	R33	Schwartz et al. (this study)
12MH06A	Takaka terrane	calc-silicate	167.3269	–45.2740	110.0	1.1	n.d.	n.d.	R33	Klepeis et al. (2016)
91-588	Western Fiordland Orthogneiss	orthogneiss	n.d.	n.d.	107.5	2.8	n.d.	n.d.	SL13	Gibson and Ireland (1995)
13NZ61	Takaka terrane	paragneiss	166.9623	–45.3208	105.6	1.9	n.d.	n.d.	R33	Schwartz et al. (this study)
12NZ11	Resolution Island Orthogneiss	hornblende orthogneiss	166.6841	–45.5989	93.0	1.6	n.d.	n.d.	R33	Hout et al. (2012)
12NZ01D	Breaksea Orthogneiss	hornblende orthogneiss	166.6367	–45.5919	92.7	2.1	n.d.	n.d.	R33	Hout et al. (2012)
13NZ33D	Breaksea Orthogneiss	hornblende orthogneiss	166.6424	–45.5922	88.8	4.7	n.d.	n.d.	R33	Klepeis et al. (2016)

(*continued*)

Faster cooling rates, as might be expected following cessation of arc magmatism and extensional orogenic collapse, would result in higher closure temperatures. For example, assuming a 100 °C/m.y. cooling rate, a 100 μm effective diffusion radius, and the Arrhenius parameters of Cherniak and Watson (2001), the zircon Pb closure temperature is 950 °C. The calculated diffusive Pb loss from the same zircon at granulite facies conditions (800–900 °C) is <5% for time scales <10 m.y. (Cherniak and Watson, 2001). Thus, for geologically young, nonmetamict zircons, diffusive Pb loss is not likely to have played a significant role relative to our analytical uncertainties even if samples were at 800–900 °C for short (<10 m.y.) periods. In interpreting zircon U-Pb isotope data, we assume that the zircon dates reflect growth with little diffusive Pb loss except where noted.

TABLE 3. SUMMARY OF ZIRCON, GARNET AND TITANITE DATES AND TEMPERATURES FOR WESTERN FIORDLAND ORTHOGNEISS AND HOST ROCKS IN WESTERN FIORDLAND, NEW ZEALAND (*continued*)

Sample	Unit	Rock type	Long.* (dd)	Lat.* (dd)	Age (Ma)	Absolute error (Ma; 2σ)	Temperature† (°C)	Absolute error (°C; 2 standard deviation)	Reference material (primary)	Reference
Metamorphic titanite chronology										
13NZ43	Takaka terrane	paragneiss	167.2533	–45.0435	113.6	2.3	853	18	BLR	Schwartz et al. (this study)
F03-59C	Malaspina pluton	orthogneiss	167.0201	–45.3608	113.4–112.1	n.d.	n.d.	n.a.	n.a.	Flowers et al. (2005)
14NZ11b	Takaka terrane	calc-silicate	167.1561	–45.2575	114.5	2.3	831	20	BLR	Schwartz et al. (this study)
					109.4	2.2	790	27	BLR	Schwartz et al. (this study)
F03-55	Takaka terrane	calc-silicate	167.0017	–45.3419	112.5–111.1	n.d.	n.d.	n.a.	n.a.	Flowers et al. (2005)
12MH06a	Takaka terrane	calc-silicate	167.3269	–45.2740	111.7	2.2	n.d.	n.a.	BLR	Schwartz et al. (this study)
13NZ61	Takaka terrane	paragneiss	166.9623	–45.3208	111.2	2.2	767	13	BLR	Schwartz et al. (this study)
13NZ41b	Takaka terrane	calc-silicate	166.8987	–45.5328	111.4	2.2	777	9	BLR	Schwartz et al. (this study)
					107.6	2.2	753	15	BLR	Schwartz et al. (this study)
12NZ13	Takaka terrane	calc-silicate	166.6861	–45.6028	110.5	2.2	841	22	BLR	Schwartz et al. (this study)
12NZ15	Takaka terrane	calc-silicate	166.6868	–45.6043	110.4	2.2	896	28	BLR	Schwartz et al. (this study)
13NZ13c	Takaka terrane	calc-silicate	166.7929	–45.6607	115.3	2.3	887	14	BLR	Schwartz et al. (this study)
					110.4	2.2	885	14	BLR	Schwartz et al. (this study)
12DC04e	Takaka terrane	paragneiss	167.1316	–45.4446	110.1	4.5	829	20	BLR	Schwartz et al. (this study)
12DC47a	Takaka terrane	calc-silicate	167.0351	–45.3574	116.0	2.3	859	32	BLR	Schwartz et al. (this study)
					110.0	2.2	n.d.	n.d.	BLR	Schwartz et al. (this study)
13NZ54	Takaka terrane	calc-silicate	167.0131	–45.1101	116.2	2.3	860	32	BLR	Schwartz et al. (this study)
					109.0	2.2	851	35	BLR	Schwartz et al. (this study)
14NZ13a	Takaka terrane	calc-silicate	167.0301	–45.2844	108.3	2.2	811	28	BLR	Schwartz et al. (this study)
					102.3	2.0	728	17	BLR	Schwartz et al. (this study)
13VA178a	Takaka terrane	calc-silicate	166.9456	–45.5129	330.1	6.6	754	19	BLR	Schwartz et al. (this study)
					104.9	7.4	699	1	BLR	Schwartz et al. (this study)
12NZ24	Misty pluton	hornblende diorite	167.1720	–45.3449	104.7	4.1	742	22	BLR	Schwartz et al. (this study)
12MH06a	Takaka terrane	calc-silicate	167.3269	–45.2740	99.2	2.0	n.d.	n.a.	BLR	Schwartz et al. (this study)
14NZ77a	Takaka terrane	amphibolite	166.8751	–45.2919	99.0	13.0	770	21	BLR	Schwartz et al. (this study)
12NZ07	Res. Island orth.	garnet orthogneiss	166.6649	–45.6051	95.2	8.9	816	16	BLR	Schwartz et al. (this study)
Metamorphic garnet chronology										
12NZ1A	Breaksea Orthogneiss	eclogite	166.6367	–45.5919	123.1	2.8	>600	n.a.	n.a.	Hout et al. (2013)
09NZ31	Malaspina pluton	garnet orthogneiss	167.0128	–45.3759	115.6	2.6	>600	n.a.	n.a.	Stowell et al. (2014)
P69531a	Malaspina pluton	garnet orthogneiss	166.8767	–45.2920	113.6	2.5	>600	n.a.	n.a.	Stowell et al. (2014)
P69531b	Malaspina pluton	garnet orthogneiss	166.8767	–45.2920	113.2	2.8	>600	n.a.	n.a.	Stowell et al. (2014)
09NZ22A	Malaspina pluton	garnet orthogneiss	167.0201	–45.4120	112.8	2.2	>600	n.a.	n.a.	Stowell et al. (2014)
09NZ29c	Malaspina pluton	garnet orthogneiss	167.0206	–45.4003	112.8	2.8	>600	n.a.	n.a.	Stowell et al. (2014)
09NZ35	Malaspina pluton	garnet orthogneiss	167.1068	–45.4138	111.9	3.0	>600	n.a.	n.a.	Stowell et al. (2014)
06NZ28	Malaspina pluton	garnet orthogneiss	166.7222	–45.7030	111.9	1.6	>600	n.a.	n.a.	Stowell et al. (2014)
09NZ17	Malaspina pluton	garnet pyroxenite	167.0017	–45.4087	111.7	3.1	>600	n.a.	n.a.	Stowell et al. (2014)
03NZDS3	Malaspina pluton	garnet orthogneiss	167.0216	–45.4118	110.6	1.9	>600	n.a.	n.a.	Stowell et al. (2014)
12NZ1A	Breaksea Orthogneiss	eclogite	166.6367	–45.5919	108.2	1.8	>600	n.a.	n.a.	Hout et al. (2013)

Note: n.d.—not determined; n.a.—not applicable.
*dd—decimal degree.
†Zircon temperatures calculated from Ti concentrations following Watson et al. (2006). Metamorphic garnet closure temperatures after Metzger et al. (1992) for garnet with radii <5 cm.
§Zircon data include isotope dilution–thermal ionization mass spectrometry and ion probe dates.

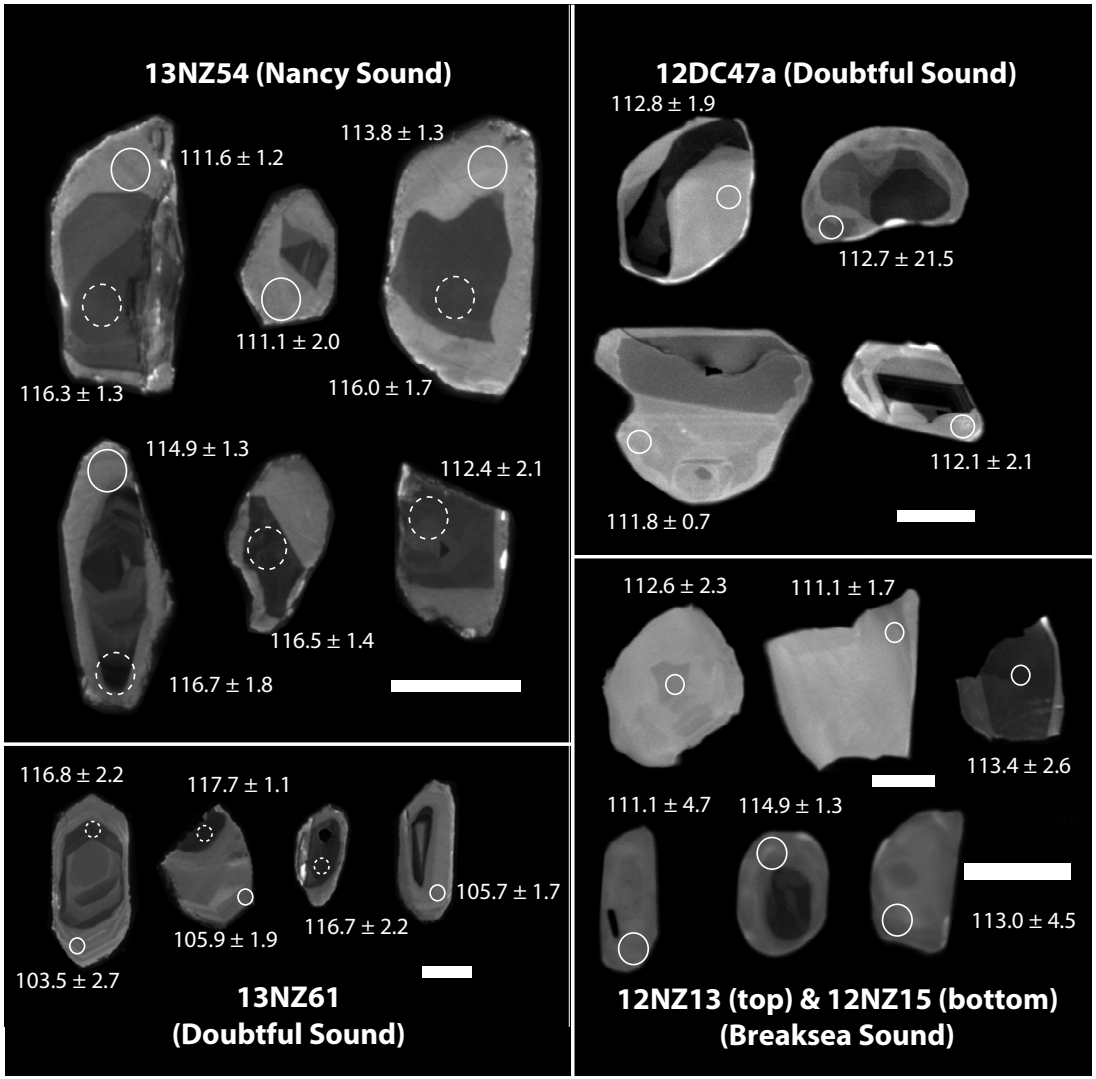

Figure 6. Cathodoluminescence images of representative metamorphic zircons in Deep Cove Gneiss from central Fiordland. Dashed and solid circles in 13NZ54 and 13NZ61 indicate interior and rim spots, respectively. Scale bars are 100 μm.

For titanite, early empirical studies of high-grade metamorphic terranes indicated a Pb closure temperature of ~500 °C (Hanson et al., 1971; Gascoyne, 1986; Tucker et al. 1987). Studies have challenged these early results and demonstrated that titanite U-Pb dates can survive high-grade metamorphism (e.g., Scott and St. Onge, 1995; Verts et al., 1996; Kohn and Corrie, 2011; Spencer et al., 2013). For example, titanite from the Himalaya preserve U-Pb dates and zirconium-in-titanite temperature information at metamorphic conditions above 750 °C (Kohn and Corrie, 2011). Spencer et al. (2013) reported orogen-wide preservation of pre-Scandian dates and zirconium-in-titanite temperatures even after long-term heating above 750 °C and at pressures well outside the stability field of titanite in the Western Gneiss region of Norway. Stearns et al. (2015) described similar findings from the Pamir Plateau, where temperatures >650 °C were sustained for at least 10 m.y. and were insufficient to reset Pb (and Zr) in titanite. An important observation in these studies is the

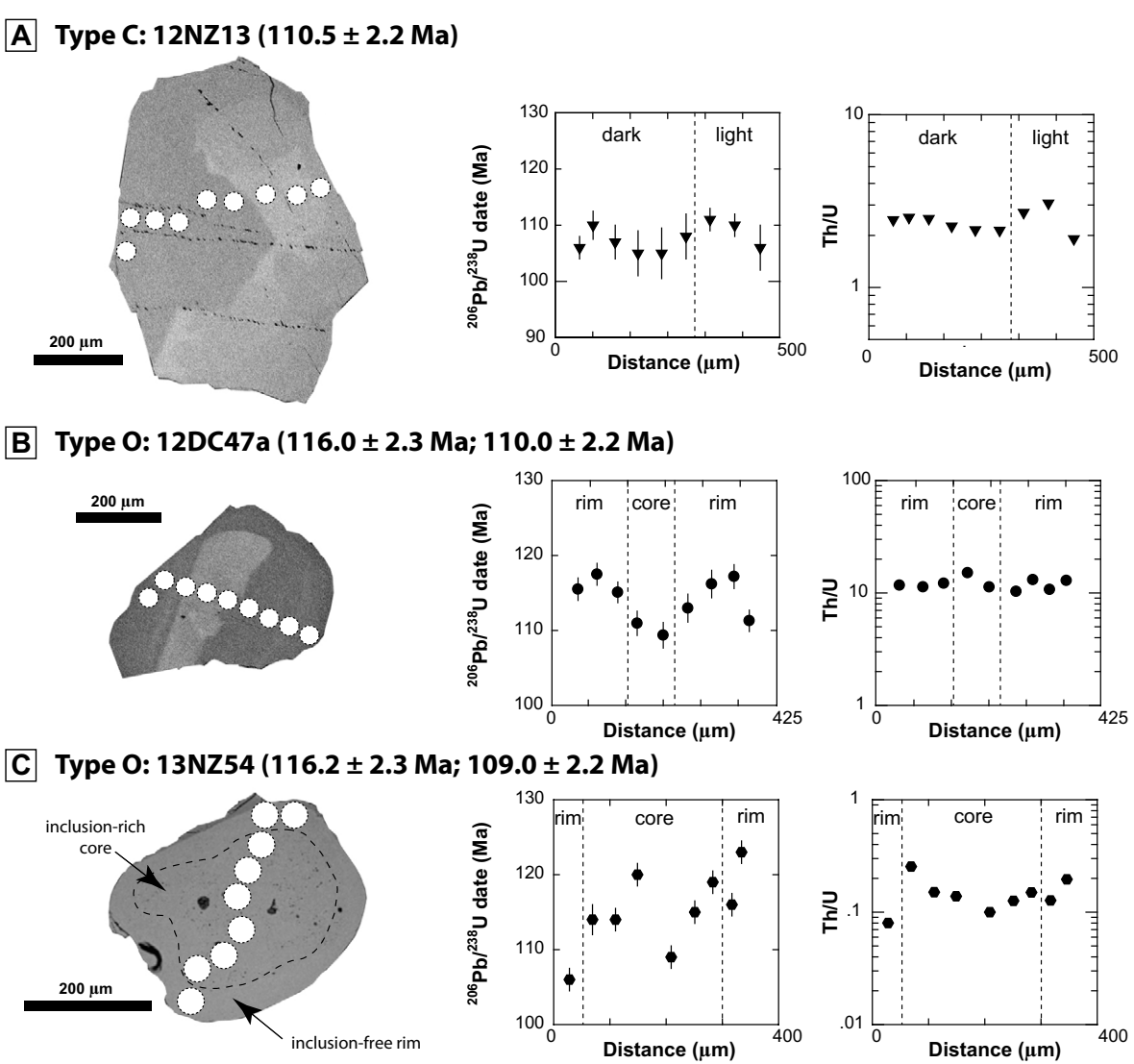

Figure 7. Backscattered electron (BSE) images of representative type C and type O titanites from Deep Cove Gneiss showing location of laser ablation–multicollector–inductively coupled plasma–mass spectrometer spots. Plots to right show rim-rim (left to right) traverses across textural boundaries. For intrasample comparison, plots show 2σ standard error internal uncertainties only for $^{206}Pb/^{238}U$ dates. (A) Type C titanites in 12NZ13 show no measurable overdispersion within error. Bright BSE region displays larger variability in Th/U values. (B) Type O titanites in 12DC47a display young (bright) core dates and older rim dates. Th/U values are weakly inversely correlated with $^{206}Pb/^{238}U$ dates. (C) Type O titanites in 13NZ54 commonly show inclusion-rich cores surrounded by inclusion-free rims. Both textural regions record a broad, overlapping distribution of dates. Th/U values show positive correlation with dates. Boundary between inclusion-rich core and inclusion-free rim domains is indicated by dashed black line.

recognition that thermally activated volume diffusion was not the principal means of U-Pb titanite resetting, but was subordinate to crystallization- or recrystallization-driven Pb mobility (Spencer et al., 2013; Stearns et al., 2015). In interpreting titanite U-Pb isotope data, we evaluate whether Fiordland titanite dates reflect new growth, prolonged crystallization or recrystallization, or volume diffusion of Pb.

Linking U-Pb dates to Zr concentrations and temperatures is an important aspect in understanding the thermal evolution of lower crust in Fiordland. Experimental studies have demonstrated that volume diffusion of Zr in titanite is ~2 orders of magnitude slower than Pb (Cherniak, 2006; Hayden et al., 2008). In Fiordland, documented peak metamorphic temperatures are reported in excess of 750 °C, indicating that Zr and Pb volume diffusion should occur.

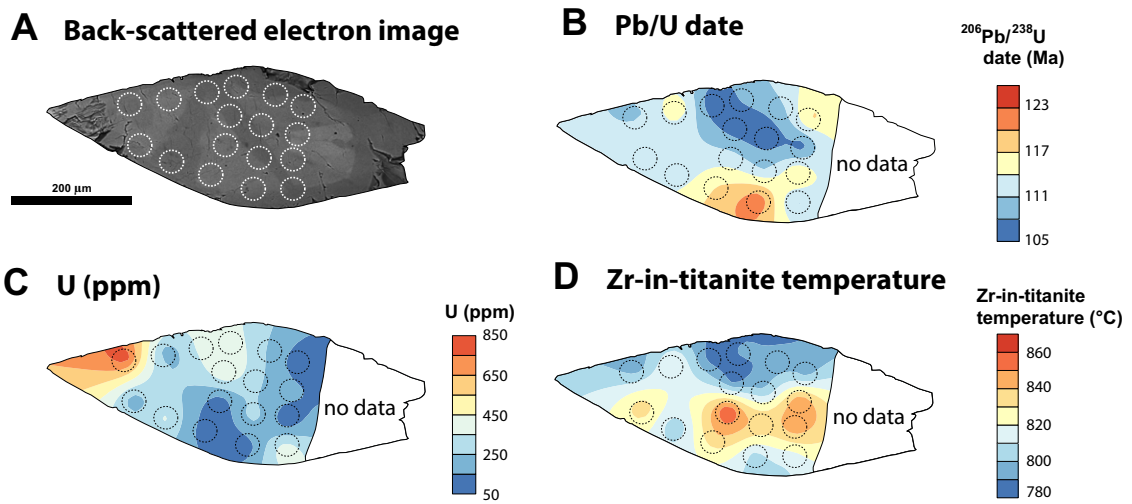

Figure 8. Textural and geochemical plots for a representative titanite grain in 14NZ13a. (A) Backscattered electron image showing complex geochemical domains whereby bright domains are characterized by higher mean atomic number. Laser ablation–multicollector–inductively coupled plasma–mass spectrometer spots are shown by dashed white circles. (B) Contour map of the same grain illustrating spatial variations in ^{207}Pb corrected $^{206}Pb/^{238}U$ dates. Note that spatial variations in dates do not correspond to simple core-rim diffusion profiles, but instead locations of young dates are suggestive of recrystallization fronts migrating from exterior to interior domains. (C) Contour map showing spatial variations in U concentration. The general pattern of dates younger than 107 Ma corresponds with intermediate U concentrations (180–460 ppm). (D) Contour map showing spatial variations in zirconium-in-titanite temperatures. In general, dates and U concentrations show a positive covariation with zirconium-in-titanite temperatures. Higher temperatures in core region may indicate preservation of an older (older than 113 Ma), low U and high Zr domain. Contoured maps were generated using Surfer 11.0 software (http://www.goldensoftware.com/products/surfer).

To evaluate the role of volume diffusion and other possible mechanisms such as new growth and/or crystallization or recrystallization, we conducted LASS grain traverses and grain mapping to evaluate links between Zr temperatures and Pb/U dates (e.g., Figs. 7 and 8).

Time-Temperature Slices

Time-temperature (*t-T*) slices of the Fiordland arc root were constructed from calculated cooling profiles using georeferenced U-Pb data from igneous zircon, metamorphic zircon, titanites, and rutile (Figs. 12 and 13; Table 3 and references therein). These time slices were constructed with the goal of aiding visualization of the transient thermal structure of the lower crust during arc-construction processes at granulite facies through extensional orogenic collapse at amphibolite facies. To construct our *t-T* slices, we assign a unique cooling path to each sample location (or node) that consists of thermochronologic data collected at that location as well as interpolated data from nearby field stations. The result is a series of time slices that integrate 26 unique *t-T* profiles across the arc root. Locations of *t-T* nodes are shown by black dots in Figure 13. Resulting temperatures from *t-T* profiles were plotted at 4 m.y. intervals and contoured in Surfer software (http://www.goldensoftware.com/products/surfer) using kriging. Metamorphic pressures are known to decrease from ~18–7 kbar in central Fiordland over the interval 116–88 Ma (Klepeis et al., 2007; DePaoli et al., 2009; Stowell et al., 2014); however, pressure changes are not clearly integrated with metamorphic ages and are therefore not incorporated in our thermal model. Given existing information, initial pressure differences from different areas within central Fiordland are probably not significant, because the Breaksea Orthogneiss and Malaspina pluton both record similar conditions of ~14–12 kbar at the initiation of our model ca. 116 Ma (DePaoli et al., 2009; Betka and Klepeis, 2013; Stowell et al., 2014). Cenozoic faulting in the region is also a source of possible error in our model; however, high-*T* chronometers yield Cretaceous Pb/U dates and are largely insensitive to late, low-*T* faulting (see House et al., 2005 for effects of Cenozoic faulting on low-*T* thermochronometers in the region). Additional details regarding *t-T* slice construction are provided in the Supplemental File text.

RESULTS

Field Observations and Sample Descriptions

Breaksea Sound and the RISZ

Batholithic rocks in the Breaksea Sound area include the Breaksea and the Resolution Orthogneisses, both of which form the footwall to the RISZ. The Breaksea Orthogneiss is a composite unit with an omphacitic granulite host (Fig. 4A) composing ~70% of exposures. Less abundant layers and pods of dark colored garnet-pyroxenite make up the remaining portion of the unit (Figs. 4A, 4B) together with sparse garnetite, clinopyroxenite, harzburgite, and hornblende peridotite. Omphacitic granulites consist of granoblastic plagioclase, garnet, omphacite, quartz, rutile, and apatite (Fig. 4C). Kyanite, ilmenite, and magnetite are found locally. Garnet pyroxenite layers and pods consist of granoblastic omphacite and garnet with lesser amounts of rutile, clinozoisite, ilmenite, magnetite, apatite, and pargasite. Titanite is absent and zircon is rare. Garnet and pyroxene layering produces a banded appearance

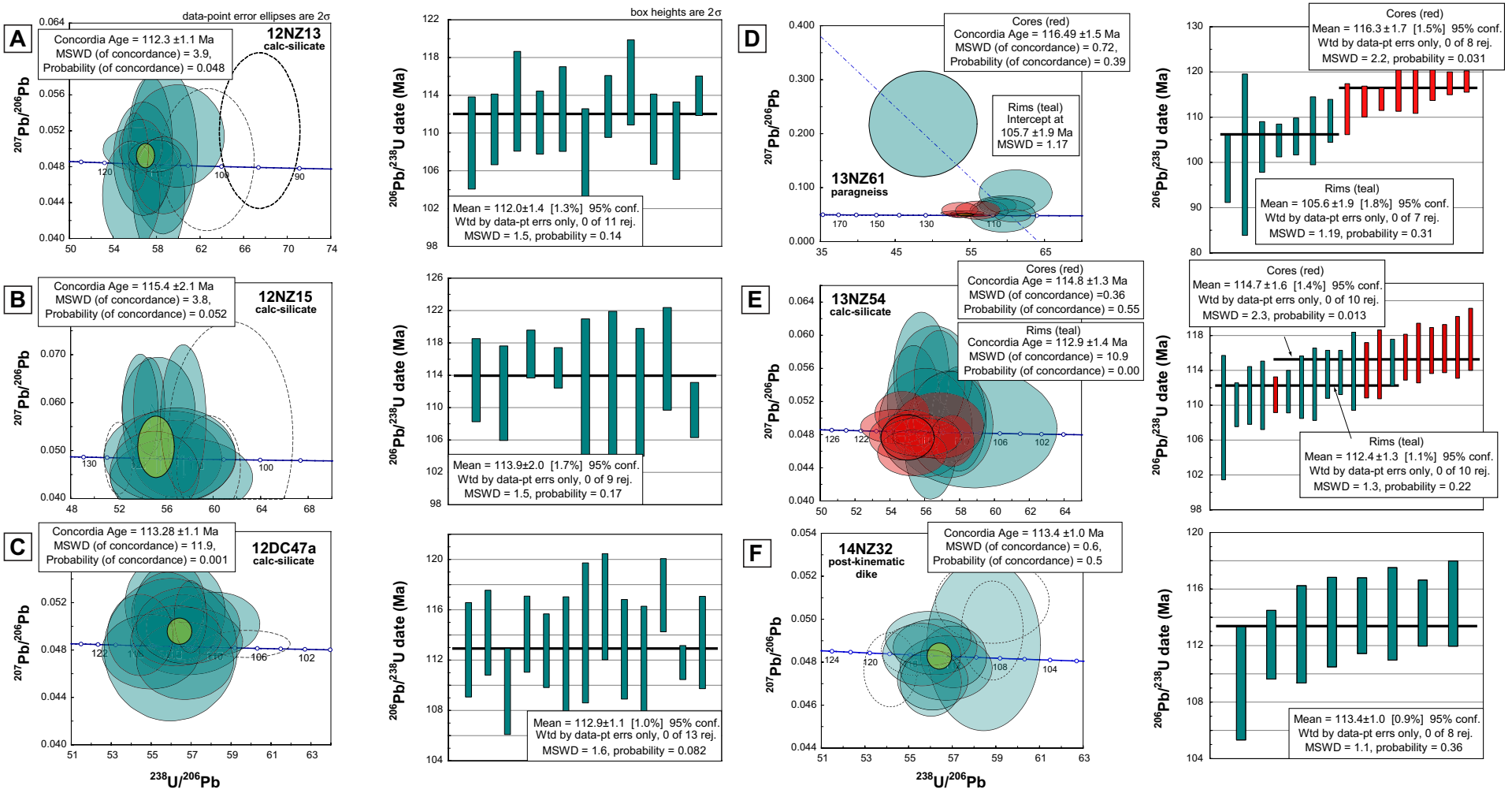

Figure 9. (A–E) Zircon concordia diagrams and weighted (wtd; pt—point; conf.—confidence; rej.—rejected) average age plots. Concordia diagrams show all analyzed spots (including rejected spots), whereas weighted average age plots show data used for age determinations (MSWD—mean square of weighted deviates). Teal and red ellipses depict individual ion probe spot analyses used in age calculations. Where multiple textural domains were analyzed, red ellipses indicate cores and/or interior domains, whereas teal ellipses represent rim domains. Yellow ellipses represent the age and uncertainty of Isoplot 3.75 generated concordia age calculations (Ludwig, 2012). Dashed white ellipses were rejected from age calculations (see text for details). Error ellipses show 2σ total uncertainty for spot analyses.

that has been interpreted to represent igneous cumulate layering of high-*P* mineral assemblages in a deep crustal MASH (melting, assimilation, storage, homogenization) zone (DePaoli et al., 2009; Clarke et al. 2013; Klepeis et al., 2016). Igneous zircon from a garnet granulite orthogneiss yielded dates ranging from 124 to 121 Ma (Hout et al., 2013; Klepeis et al., 2016) and is interpreted as recording the timing of magmatic construction of this unit.

The Resolution Orthogneiss consists of hornblende metadiorite and metagabbro (Fig. 4D) that intrude the Breaksea Orthogneiss. Granoblastic metadiorite contain hornblende, plagioclase, clinozoisite, ilmenite, magnetite, quartz, apatite, and rutile. Biotite and titanite are sometimes present; fine-grained metamorphic garnet and clinopyroxene are also present, but are typically less abundant than in the Breaksea Orthogneiss. Titanite occurs as

a secondary, retrogressive phase often overgrowing ilmenite and/or rutile. Secondary green hornblende also overgrows titanite. In unstrained zones, alternating layers of hornblende and plagioclase display grading suggesting density sorting during magmatic crystallization. Hout et al. (2013) reported a $^{206}Pb/^{238}U$ zircon date of 115.1 ± 1.6 Ma from an undeformed hornblende diorite.

Early igneous fabrics in the Breaksea and Resolution Orthogneisses are overprinted by a high-*T* migmatitic fabric that developed during eclogite to garnet granulite facies metamorphism (Fig. 4C). At the entrance to Breaksea Sound, kilometer-scale gneiss domes occur in eclogites and omphacitic granulites and are defined by complex, nearly concentric foliation trajectories previously interpreted to reflect buoyancy-driven flow in melt-rich zones (see Betka and Klepeis, 2013, and Klepeis et al., 2016, for detailed discussion of gneiss dome kinematics). Constrictional flow fabrics are dominant and are associated with dome formation. Mineral lineations in L > S domains are defined by aligned aggregates of plagioclase, pyroxenes, and/or hornblende. Migmatitic leucosomes are common in omphacitic granulites and occur with large (1–3 cm) peritectic garnets.

Retrogressive, upper amphibolite facies metamorphism resulted in the development of gneissic and locally mylonitic shear zones, particularly at contacts between the Breaksea and Resolution Orthogneisses (footwall) and the Deep Cove Gneiss (hanging wall). The RISZ is the largest of these shear zones in the Breaksea area and ranges from 200 to 500 m in thickness (Betka and Klepeis, 2013; Figs. 4D and 5A). In the hanging wall of the RISZ, the Deep Cove Gneiss consists of biotite- and hornblende-bearing gneisses interlayered with quartzite, marble, calc-silicates, and schist. Within the shear zone, Deep Cove Gneiss exhibits a penetrative, upper amphibolite facies L > S fabric consisting of hornblende-clinozoisite-biotite gneiss that is complexly interfolded with calc-silicate and amphibolite. Garnet and pyroxene are absent from mafic gneisses, suggesting that they were unstable under higher fluid activity conditions during amphibolite facies retrogression. Calc-silicates display a range of assemblages including calcite, plagioclase, diopside, quartz, garnet, titanites, and zircon. Mylonitic fabrics are common in the marbles and calc-silicates; however, granoblastic textures are locally present. Two examples of calc-silicates were collected from the RISZ at the entrance to Breaksea Sound (12NZ13 and 12NZ15) and a footwall sample (12NZ07) was collected from the Resolution Orthogneiss.

Doubtful Sound and DSSZ

In the Doubtful Sound region, the WFO consists of two large dioritic to monzodioritic intrusive units termed the Malaspina and Misty plutons (Fig. 2). They are separated by the Paleogene–Neogene Wilmot fault; however, in Cretaceous reconstructions, they formed the footwall and hanging wall, respectively, to the DSSZ (Fig. 1B, inset). The Malaspina pluton consists of diorite, hornblende diorite, and monzodiorite. Scarce hornblendite and pyroxenite are present. Igneous mineral assemblages include plagioclase and hornblende, with lesser amounts of clinopyroxene, orthopyroxene, biotite, apatite, quartz, and zircon. Titanite is occasionally present as a secondary phase. Original igneous foliations are recognized by layering of coarse hornblende and clinopyroxene within a plagioclase matrix. Aligned clots of hornblende and clinopyroxene are also present and may represent enclaves related to mafic recharge. Intrusive contacts between the Malaspina pluton and the Deep Cove Gneiss are commonly overprinted by amphibolite facies extensional shear zones (see following). In rare cases original intrusive contacts are preserved, such as in Wet Jacket Sound (at location 13NZ13c) and in western Crooked Arm. Contacts between the Malaspina pluton and the Breaksea Orthogneiss were not observed in this study; however, xenoliths of garnet-pyroxenite as much as 10 m wide occur as rafts within the Malaspina pluton along the eastern shore of Acheron Passage, suggesting that intrusion of the Malaspina pluton disrupted high-*P* mineral cumulates at the base of the arc.

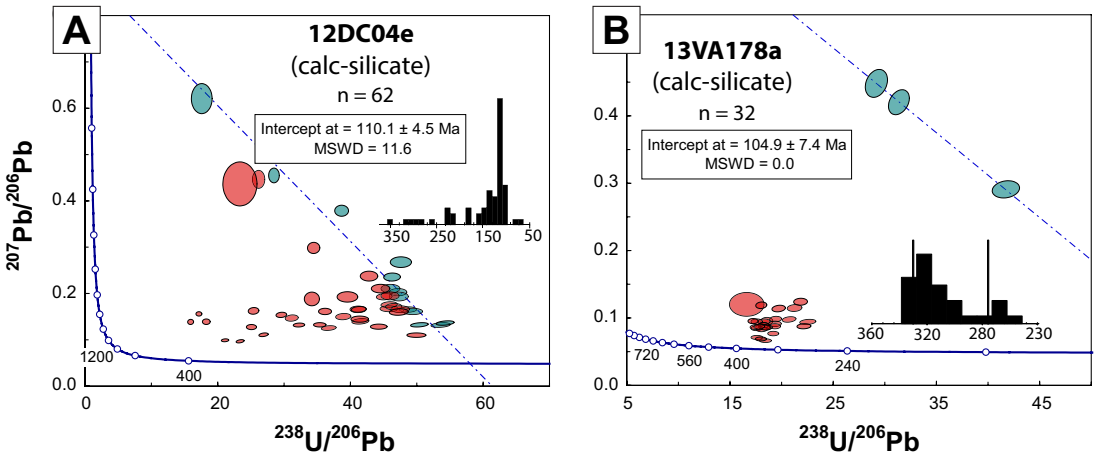

Figure 10 (*on this and following two pages*). Titanite concordia diagrams and histograms. Thin vertical black lines in histogram indicate peak age populations calculated from the Sambridge and Compston (1994) multicomponent unmixing algorithm. (A, B) Type P titanites preserve mostly pre-Cretaceous dates.

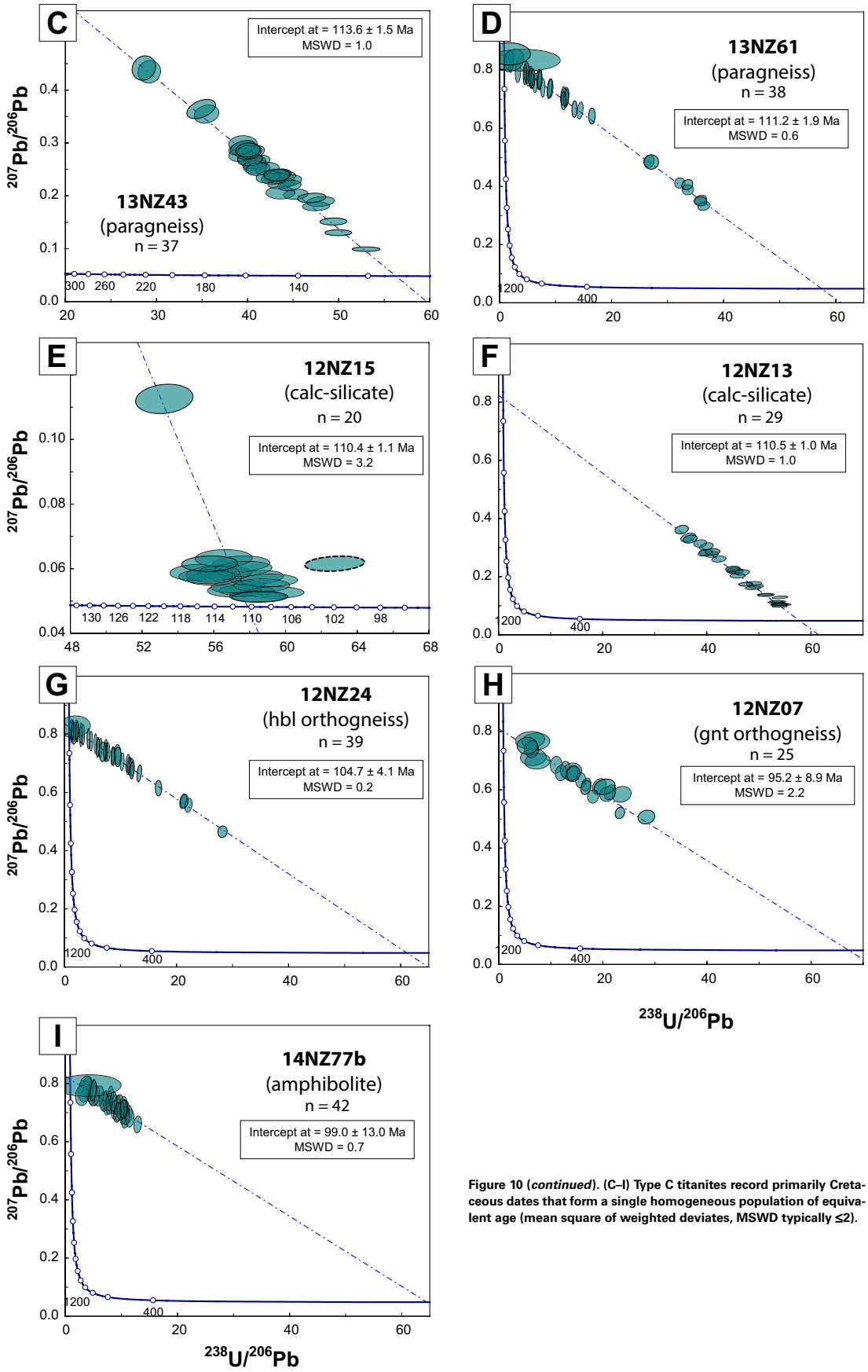

Figure 10 (*continued*). (C–I) Type C titanites record primarily Cretaceous dates that form a single homogeneous population of equivalent age (mean square of weighted deviates, MSWD typically ≤2).

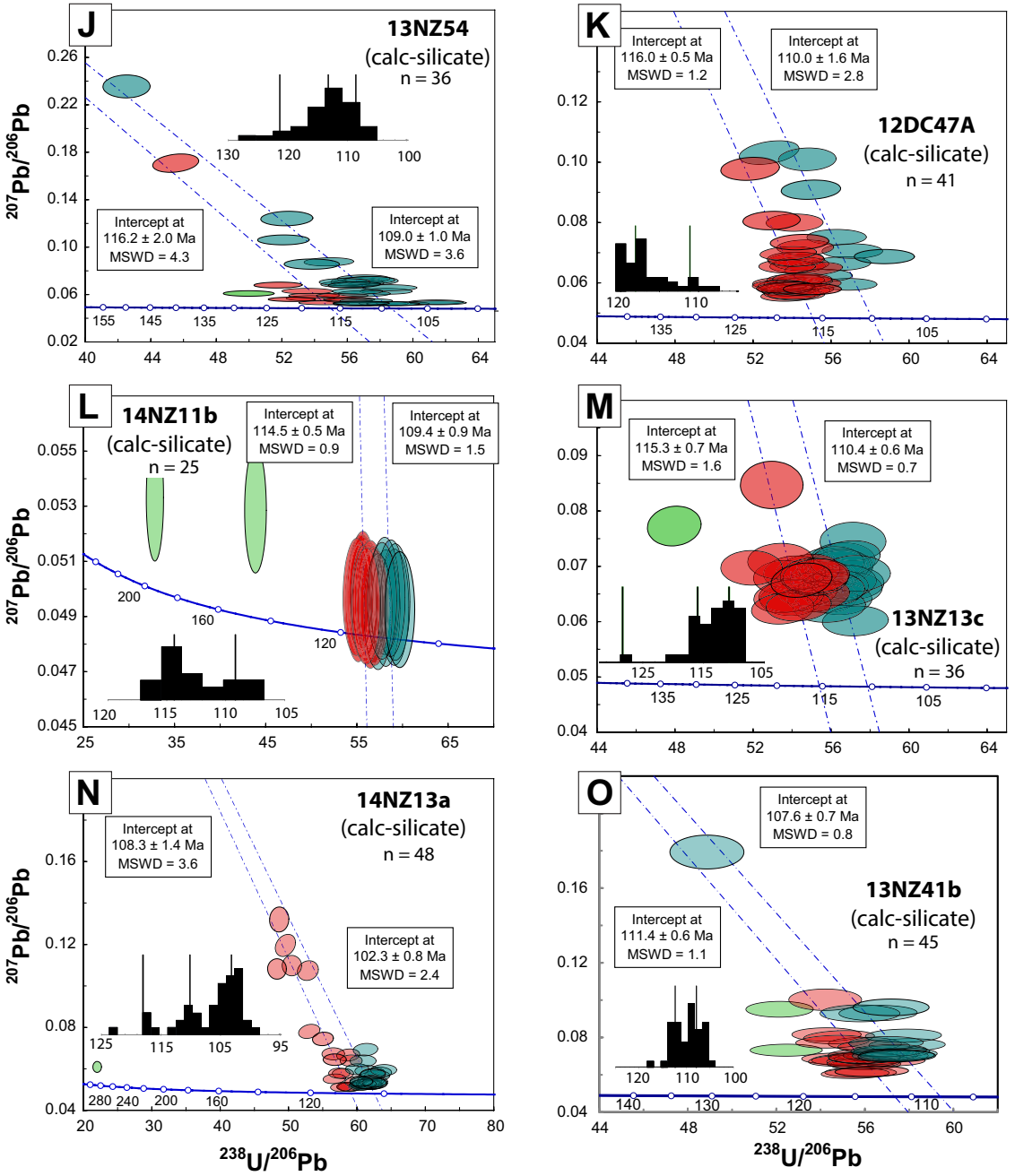

Figure 10 (*continued*). (J–O) Type O titanites are characterized by an overdispersion of Cretaceous dates spanning 5–10 m.y. or more. Error ellipses show 2σ total uncertainty for spot analyses. Calculated intercept age uncertainties are reported at the 95% confidence interval and include analytical and decay constant errors; the total uncertainty (analytical + systematic + decay constant) for any one date is 2% (or 2.2 m.y. at 110 Ma).

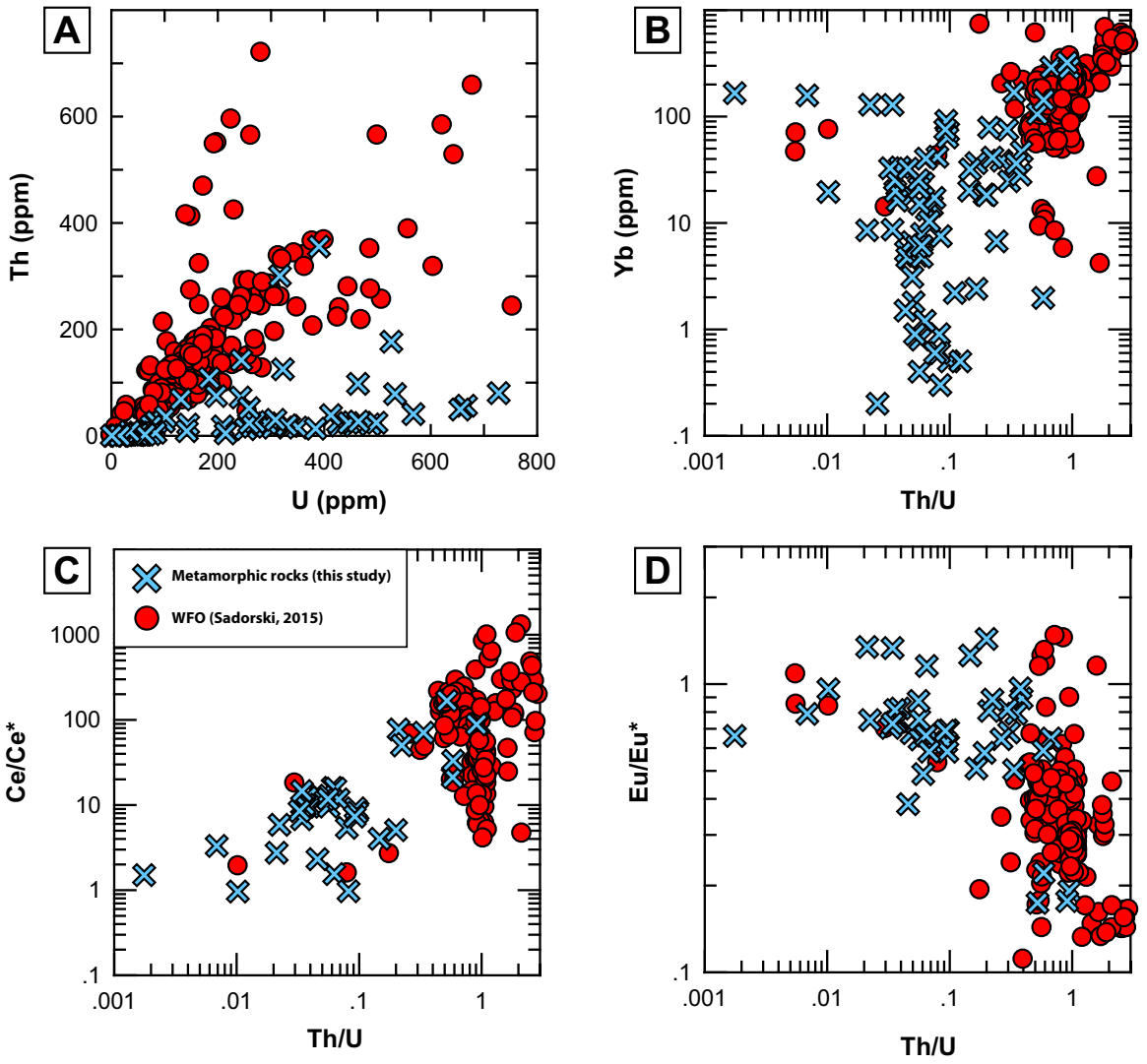

Figure 11. Zircon trace element geochemistry plots illustrating chemical distinctions between igneous and metamorphic zircons. With the exception of one sample (13NZ61), metamorphic zircons have low Th/U values (typical < 0.1) that distinguish them from Western Fiordland Orthogneiss (WFO) zircons. Relative to igneous zircons, metamorphic zircons display lower Th (<100 ppm; Fig. 10A), Yb (<100 ppm; Fig. 10B), lower Ce/Ce* (<100; Fig. 10C), and higher average Eu/Eu* values (>0.5; Fig. 10D). Data signify that zircons from metamorphic rocks in extensional shear zones adjacent to the WFO are not tectonically mixed igneous zircons, but rather represent new growth following or during WFO emplacement.

The Misty pluton consists of medium-grained two-pyroxene diorite, hornblende diorite, and monzodiorite with minor monzonite. Apatite, zircon, magnetite, and ilmenite are common accessory phases, and titanite is rare except in retrograde amphibolite facies assemblages. Locally, the Misty pluton displays compositional banding composed of dioritic gneiss and centimeter- to meter-scale layers of hornblendite. In some cases, angular brecciated hornblendite clasts are surrounded by diorite, suggesting that emplacement of the Misty pluton involved magma fracturing of brittle hornblendite (Fig. 4E). U-Pb zircon dating of the Misty and Malaspina plutons indicates that both units were emplaced contemporaneously from ca. 120 to 115 Ma (Sadorski, 2015).

Garnet granulite facies metamorphism of both the Malaspina and Misty plutons resulted in transposition of earlier magmatic fabrics and recrys-

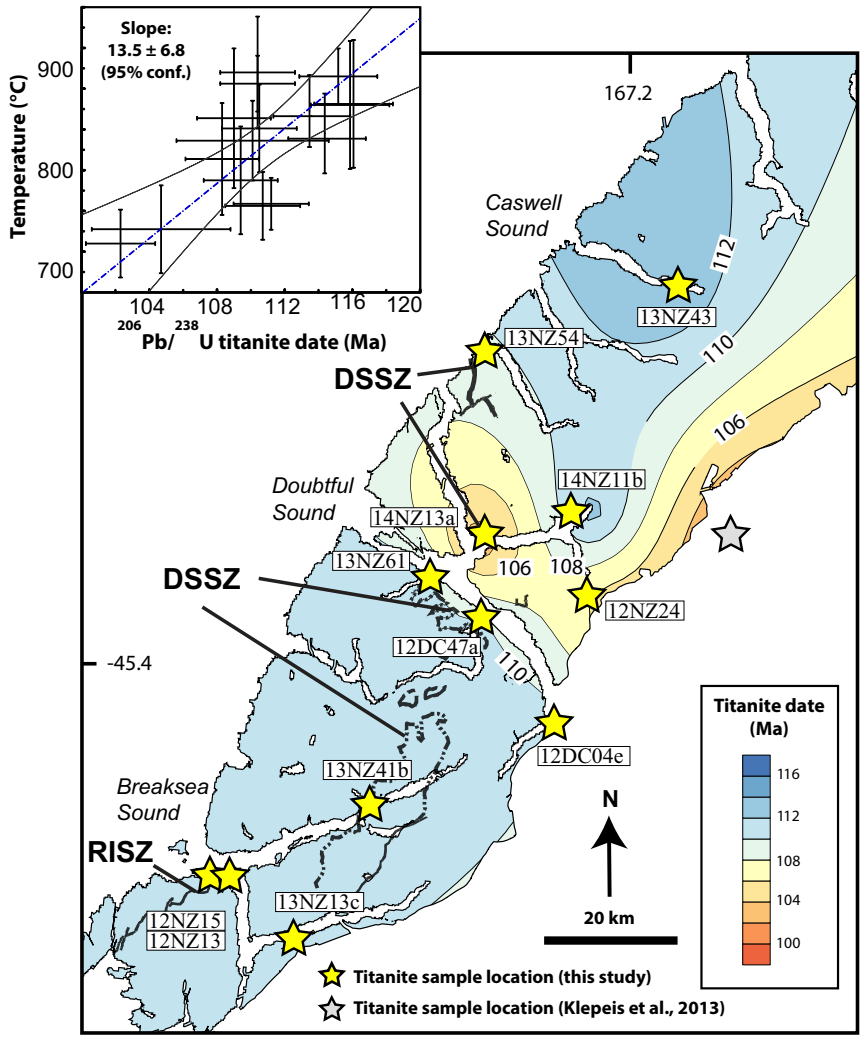

Figure 12. Contoured titanite age variation map constructed using youngest peak age in each sample. Map excludes samples with Paleozoic titanite populations (13VA178a) and those with large uncertainties (12NZ07, 14NZ77b). Note that some regions are undersampled or data lack sufficient age resolution to be meaningful (e.g., western Malaspina pluton and eastern Misty pluton). Spatial distribution of high-resolution data shows widespread pattern of granulite facies metamorphism ca. 113–108 Ma, followed by an apparent geographically localized pulse from 106 to 102 Ma. Sustained high-temperature heating may have been driven by post–Western Fiordland Orthogneiss (WFO) mafic underplating related to foundering of a high-density arc root and/or asthenospheric upwelling related to extensional thinning. Locations of Doubtful Sound shear zone (DSSZ) and Resolution Island shear zone (RISZ) are indicated. Inset shows time-temperature plot of all titanite populations in this study (conf.—confidence). Least squares regression of all titanite data yield slow cooling rates of 13.5 ± 6.8 °C/m.y. over the temperature range of 900–700 °C.

tallization associated with the development of garnet and clinopyroxene coronas and coarse ribbons of dynamically recrystallized plagioclase + clinopyroxene + garnet aggregates (Fig. 4C). Metamorphic garnet occurs as three distinct textural types that reflect (1) fine-grained garnet + clinopyroxene intergrowths in dehydration zones; (2) coarse porphyroblasts within trondhjemitic leucosome veins; and (3) coarse porphyroblasts surrounded by plagioclase-rich halos without leucosome veins (Stowell et al., 2014) (Fig. 4F). In the Malaspina pluton, stromatic migmatite zones in the footwall to the DSSZ display mylonitic textures that are cut by garnet-bearing leucosome veins, indicating that partial melting and deformation were synchronous. In the Misty pluton, S_2 foliations in two-pyroxene diorites are truncated by garnet-bearing leucosomes that show a coarsening of hornblende adjacent to leucosome margins (Fig. 4G). Garnet appears within the leucosome and in the selvage region. Hornblende reaction zones are interpreted to reflect hydration of the host pyroxene diorite during hydrous melt migration through leucosome veins.

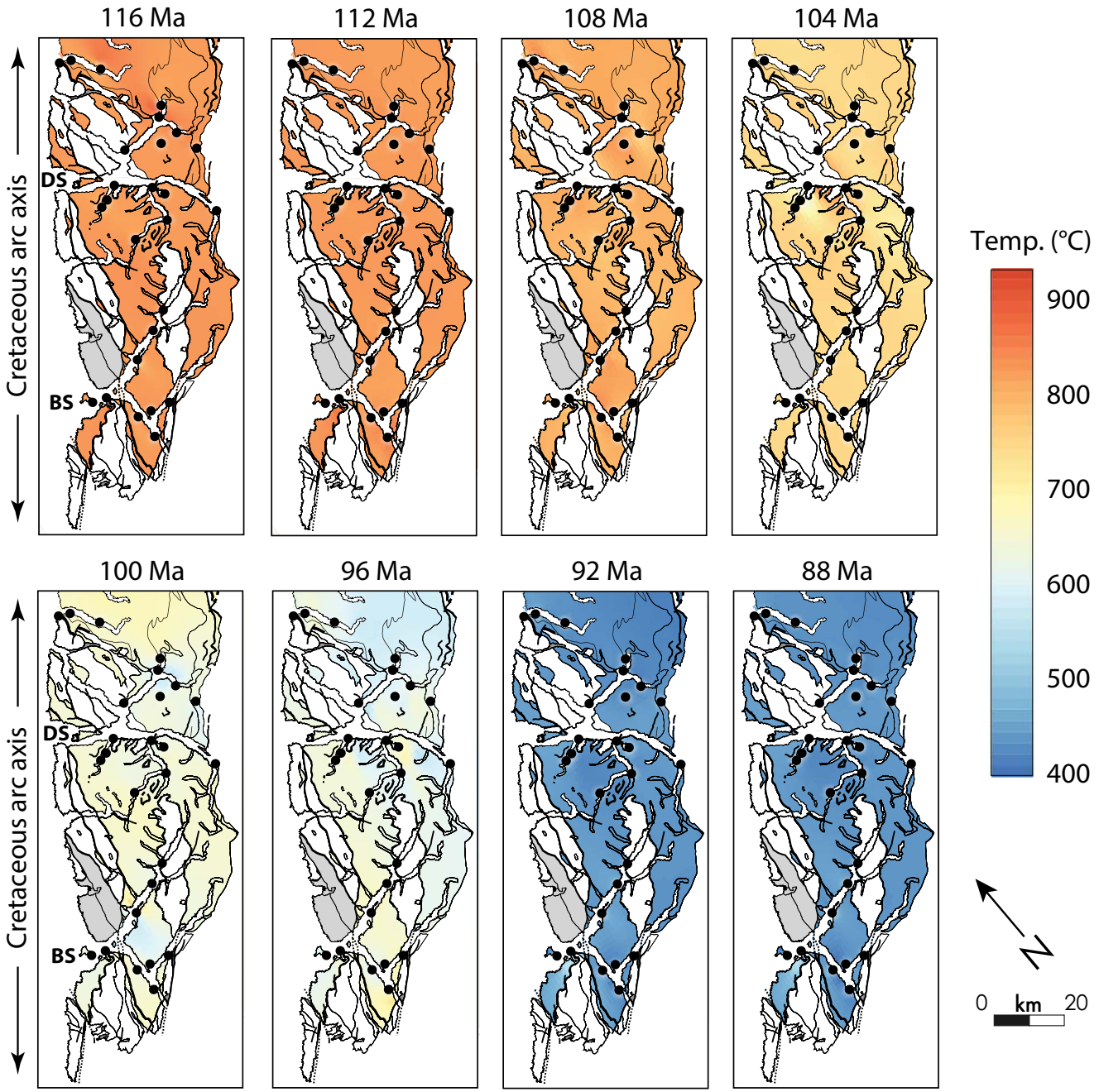

Figure 13. Time-temperature (Temp.) maps of Fiordland arc root at 4 m.y. time slices. Maps were generated using $^{206}Pb/^{238}U$ igneous zircon dates and titanium-in-zircon thermometry from Sadorski (2015), zircon and titanite chronology and thermometry data (this study), and rutile dates (Clements et al., 2014). Time-temperature maps show the final phases of Western Fiordland Orthogneiss (WFO) emplacement at 116 Ma, widespread granulite facies metamorphism (112–108 Ma), and localized sustained heating (or reheating) at 106–100 Ma in the southeastern lobe of the Misty pluton in the Doubtful Sound region.

Progressive hydration and retrogression of earlier, garnet granulite facies fabrics is preserved in upper amphibolite facies fabrics in the DSSZ (e.g., Figs. 5B–5D). S_3 foliations in amphibolite facies high-strain zones are commonly shallowly dipping and defined by aligned clusters of hornblende, plagioclase, epidote, and locally biotite and titanite. Hydrous minerals commonly exhibit evidence for extensive neoblastic growth and complete replacement of garnet and clinopyroxene. In the hanging wall of the DSSZ, paragneisses have tight, recumbent folds (e.g., Fig. 5B), implying that a component of nearly vertical shortening accompanied horizontal flow (Klepeis et al., 2007, 2016). Kinematic analysis suggests that subhorizontal (northeast-southwest) extension was accommodated by approximately equal amounts of pure and simple shear as strain was progressively localized into networks of thin, conjugate-style shear zones (Klepeis et al., 2007, 2016). Six samples were collected from paragneisses and calc-silicates within the DSSZ in Doubtful Sound and east of Breaksea Sound (13NZ41b, 12DC04e, 12DC47a, 13NZ61, 14NZ77b). Splays of the DSSZ also occur at the entrance to Nancy Sound and Bradshaw Sound (e.g., 13NZ54 and 14NZ13a). Upper amphibolite facies metamorphic fabrics also occur in the hanging wall of the DSSZ (e.g., 12NZ24) and are not always associated with deformational textures (Fig. 4H).

Caswell Sound

Evidence for contractional deformation is preserved in Caswell Sound (Fig. 2), where a bivergent thrust system emplaced the Caswell Gneiss and Western McKerr intrusives over the Misty pluton (Daczko et al., 2002; Klepeis et al., 2004). The Caswell Gneiss consists of calc-silicate, marble, paragneiss (13NZ43), and schist complexly interlayered with biotite metadiorite. The Western McKerr intrusives consist of two-pyroxene diorite, pyroxene monzodiorite, quartz monzodiorite, and monzodiorite (Allibone et al., 2009a). Both units are thrust over the Misty pluton along granulite to amphibolite facies, ductile thrust faults defined by mylonitic to ultramylonitic fabrics (Daczko et al., 2002). Sadorski (2015) reported an age of 116.9 ± 1.2 Ma for a footwall sample of the Misty pluton, and Klepeis et al. (2004) reported a similar date of 116.8 ± 3.7 Ma for an imbricated hanging-wall sample of the Western McKerr intrusives. These dates suggest that the two units are coeval and likely represent the imbricated roof of the Misty pluton. Postkinematic, granitic A-type dikes cut these fabrics (14NZ32) and were sampled to place a lower limit on the timing of contractional deformation in the WFO.

Zircon SHRIMP-RG Chronology

Zircons are typically <200 µm in length, anhedral, and stubby with aspect ratios of 1:1–2:1. They are clear and colorless, and lack visible mineral inclusions. In SEM-CL imaging, they display very weak oscillatory zoning (Fig. 6). In many samples, chemically distinct, high-U cores are embayed and interior zonation is truncated by overgrowths of lower U rim domains, suggesting multiple phases of growth during changing chemical environments (e.g., 13NZ61 and 13NZ54 in Fig. 6). In this study we target both core and rim domains to evaluate time scales of zircon growth. Ages are weighted average ages unless otherwise specified.

Two calc-silicate samples were collected from within the RISZ (12NZ15 and 12NZ13 in Fig. 2). For sample 12NZ13, 13 individual SHRIMP-RG spot analyses on separate zircon grains yield a $^{206}Pb/^{238}U$ age of 110.6 ± 3.1 Ma (mean square of weighted deviates, MSWD = 7.2). Two spots give anomalously young dates of 94 and 102 Ma, and likely underwent Pb loss. The remaining 11 zircons yield a $^{206}Pb/^{238}U$ age of 112.0 ± 1.4 Ma (MSWD = 1.5; Fig. 9A).

Individual SHRIMP-RG spot analyses (n = 12) from 12 zircons in 12NZ15 yield a $^{206}Pb/^{238}U$ age of 115.1 ± 3.3 Ma (MSWD = 6.8). The overdispersion of dates indicates a component of nonanalytical scatter in the data. One spot analysis from a rim domain is slightly older (122 Ma) than the rest of the analyses and two other zircons yield younger apparent dates of 103 and 107 Ma. Excluding these three spots results in a $^{206}Pb/^{238}U$ age of 113.9 ± 2.0 Ma (MSWD = 1.5; Fig. 9B).

Zircons from a calc-silicate (n = 14) within the DSSZ (12DC47a) yielded a $^{206}Pb/^{238}U$ age of 112.5 ± 1.4 Ma (MSWD = 2.6). One spot has anomalously high U concentration (3432 ppm) and a young apparent date of 107 Ma. Given the high U concentration, we cannot rule out the possibility of matrix effects or Pb loss affecting this zircon (e.g., White and Ireland, 2012); this date is therefore excluded from further consideration. The remaining 13 zircons yield a $^{206}Pb/^{238}U$ age of 112.9 ± 1.1 Ma (MSWD = 1.6; Fig. 9C).

Zircons from a paragneiss (13NZ61) also within the DSSZ display well-developed core and rim textures (Fig. 6). The $^{206}Pb/^{238}U$ dates for nine cores are all Cretaceous with the exception of one Precambrian date of 1430 Ma, which is the only non-Cretaceous zircon analyzed in this study. The age of all cores, excluding the Precambrian outlier, is 116.3 ± 1.7 Ma (MSWD = 2.2; Fig. 9D). The age of seven rim spot analyses is 105.6 ± 1.9 Ma (MSWD = 1.2; Fig. 9D). Core domains are also chemically distinct from rims and on average have higher U (131–526 ppm) and Th/U values above 0.2 compared to rims (U = 1–35 ppm; Th/U < 0.1).

A calc-silicate from within a splay of the DSSZ at the entrance to Nancy Sound (13NZ54) also displays core and rim textures in CL images (Fig. 6). Individual spot analyses (n = 10) from zircon cores yield an age of 114.7 ± 1.6 Ma (MSWD = 2.3); 10 spots from 10 rim domains yield an overlapping age within uncertainty of 112.4 ± 1.3 Ma (MSWD = 1.3; Fig. 9E). Cores and rims are chemically distinct, with rims characterized by lower average U concentrations (43–83 ppm) relative to cores (142–533 ppm). Both cores and rims have overlapping Th/U values ≤0.1.

A postkinematic dike from the Caswell Sound fold-thrust belt (14NZ32) yielded 12 spot analyses ranging from 118.1 to 108.3 Ma (Fig. 9F). The 2 spots that yielded the oldest dates (115.6–118.1 Ma) have extremely high U concentrations ranging from 4000 to 4700 ppm and may have older ages due to matrix effects (e.g., White and Ireland, 2012); we therefore exclude these dates. The remaining samples yield a weighted average age of 112.2 ± 1.8 Ma (MSWD = 3.2). One of the youngest spots is discordant and another does not

overlap with the majority of other spots in Tera-Wasserburg space (dashed spots at 108 Ma in Fig. 9F). Excluding these spots results in a weighted average age of 113.4 ± 1.0 Ma (MSWD = 1.1). We prefer this age for the timing of dike emplacement.

Zircon SHRIMP-RG Geochemistry

Zircons within extensional shear zones are distinct from those in footwall rocks of the WFO (Fig. 11). They are characterized by extremely low light rare earth element concentrations commonly below 1 ppm for La, Ce, and Nd (see Supplemental File text). They have low average Th/U values (<0.4), and Th (<100 ppm) and Yb (<60 ppm) concentrations (Fig. 11). On average, Ce/Ce* values are <100 and Eu/Eu* values are >0.5.

Titanite Laser Ablation–Multicollector–ICP-MS Chronology

Titanites from calc-silicates, paragneisses, and orthogneisses typically display patchy zoning in BSE images (Figs. 7 and 8) that reflect growth and/or crystallization or recrystallization involving reactions with Ca- and Al-bearing phases such as calcite, clinopyroxene, plagioclase, epidote, and hornblende (Franz and Spear, 1985; Essex and Gromet, 2000; Hayden et al., 2008; Kohn and Corrie, 2011; Spencer et al., 2013; Bonamici et al., 2014; Stearns et al., 2015). Laser ablation–multicollector–ICP-MS spots were selected to investigate the temporal patterns associated with the textural relationships observed in BSE images. The metamorphic titanites commonly yield isotopic ratios that define isochrons in Tera-Wasserburg space (e.g., Figs. 10C–10I). Many samples, however, show more complex U-Pb ratios that do not define an isochron (MSWD >> 1). Within these samples, we observe: (1) titanite populations that preserve a wide range of $^{206}Pb/^{238}U$ dates ranging from Mississippian to Cretaceous (e.g., 13VA178a and 12DC04e) and (2) titanite populations that display only Cretaceous dates, but yield an overdispersion spanning 5–10 m.y. or more (Figs. 10J–10O). Samples that preserve pre-Cretaceous dates are located in the hanging wall of extensional faults at significant distances (500 m or more) above contacts with the WFO (sample 13VA178a), or at the margins of the WFO (sample 12DC04e). We classify titanites according to their distribution of dates as follows: type P titanites preserve mostly pre-Cretaceous dates (Figs. 10A, 10B); type C titanites record primarily Cretaceous dates that form a single, homogeneous population of equivalent age (MSWD typically ≤ 2: Figs. 10C–10I); and type O titanites display an overdispersion of Cretaceous dates spanning 5–10 m.y. or more (Figs. 10J–10O).

Type P: Pre-Cretaceous Titanites

A sample from the easternmost margin of the WFO in the DSSZ (12DC04e) yields a large population of mixed, but mostly pre-Cretaceous $^{206}Pb/^{238}U$ dates ranging from ca. 355 Ma to 100 Ma. Though mostly pre-Cretaceous, this sample also contains a Cretaceous population with a lower intercept of 110.1 ± 4.5 Ma (Fig. 10A) and a large MSWD. Another sample, 13VA178a, located >500 m structurally above the DSSZ, contains mostly Mississippian dates with a peak population of 330.1 ± 6.6 Ma, and 3 grains that define a poorly constrained isochron age of 104.9 ± 7.4 Ma (Fig. 10B). The latter date is based on only three grains and is not discussed further. Two samples from Bradshaw Sound also contain minor (n = 3) pre-Cretaceous titanites with dates of 146 Ma and 196 Ma (14NZ11b) and 285 Ma (14NZ13a; see Supplemental File text). These two samples also contain Cretaceous populations and are discussed in more detail in the following.

Type C: Homogeneous Cretaceous Titanite Population

Nearly half of samples in this study yield homogeneous titanite populations with lower intercept dates clustering at 114–110 Ma (Figs. 7A and 10C–10I). For example, in the Caswell Sound fold-thrust belt, titanites from a paragneiss (13NZ43) give a well-defined isochron of 113.6 ± 2.3 Ma (Fig. 10C). Within the DSSZ, titanites from a paragneiss at the entrance to First Arm (13NZ61) give a date of 111.2 ± 2.2 Ma (Fig. 10D). Two calc-silicates from within the RISZ (12NZ15 and 12NZ13) give identical dates of 110.4 ± 2.2 Ma and 110.5 ± 2.2 Ma (Figs. 10E, 10F). An orthogneiss from the hanging wall of the DSSZ (southeastern lobe of the Misty pluton; 12NZ24) has a strong amphibolite facies overprint and a younger date of 104.7 ± 4.1 Ma (Fig. 10G). Two samples have low radiogenic Pb/common Pb values and yield young dates of 95.2 ± 8.9 Ma (Fig. 10H) and 99.0 ± 13.0 Ma (Fig. 9I). Although these dates are the youngest observed in this study, we are cautious in interpreting their significance due to their large uncertainties (9%–13%, 2σ). Consequently, these dates are not emphasized or used in generating contoured plots (Figs. 12 and 13).

Type O: Overdispersed Cretaceous Titanite Population

Of the samples, 40% (6 of 15) display overdispersed titanite dates for which MSWD values are >>1 (Figs. 10J–10O). Using the Sambridge and Compston (1994) algorithm, individual samples yield peak titanite populations ranging from ca. 116 to 108 Ma (Table 2). In some cases, titanite populations are normally distributed (e.g., 13NZ54; Fig. 10J), but the majority of samples have continuous to bimodal date populations (e.g., 12DC47a; Fig. 10K). With the exception of 14NZ13a (see following), the oldest populations give dates ranging from 116.2 ± 2.3 to 114.5 ± 2.3 Ma, and younger populations yield dates ranging from 110.4 ± 2.2 to 107.6 ± 2.2 Ma (Table 2). Sample 14NZ13a (splay within the DSSZ) is an exception and yields overdispersed dates with peak populations at 108.3 ± 2.2 and 102.3 ± 2.0 Ma (Fig. 10N).

In general, the overdispersed dates do not correlate with simple core-rim growth textures (e.g., type O titanites in Figs. 7B, 7C). For example, in sample 12DC47a (DSSZ), two spots in the core of one titanite yield young dates of 109.4 ± 1.4 and 110.9 ± 1.5 Ma (2σ SE internal uncertainties), and are surrounded by older interior and rim domain dates as old as 117.5 ± 1.4 Ma (Fig. 7B). The weighted average date of all nine spots on this grain is 114 ± 2.2 Ma

(MSWD = 14). In sample 13NZ54 (splay of DSSZ), BSE images reveal inclusion-rich cores surrounded by inclusion-free rims; however, both domains give overlapping dates ranging from 119.5 ± 1.8 Ma to 105.8 ± 1.2 Ma for inclusion-rich cores, and 123.1 ± 1.5 Ma to 105.8 ± 1.4 Ma for inclusion-free rims (Fig. 7C). SEM–energy-dispersive X-ray spectroscopy results indicate that inclusions are primarily plagioclase feldspar. A titanite from 14NZ13a (Figs. 8A–8D) also displays a complex spatial distribution with young dates (107–105 Ma) forming apparent domains that extend from exterior to interior portions of the grain. The oldest date in this grain (122.4 ± 1.6 Ma) is located in an exterior domain (Fig. 8B). Collectively, the spatial variation in dates is not consistent with expectations for thermally mediated volume diffusion. Instead, we argue that the overdispersion reflects incomplete or prolonged intragrain recrystallization.

Titanite Thermometry

Type P, pre-Cretaceous titanites in a hanging-wall calc-silicate above the DSSZ (13VA178a) yield a temperature of 754 °C. Another type P titanite sample in the DSSZ (12DC04e) gives a temperature of 859 °C for pre-Cretaceous titanites and 829 °C for the ca. 110 Ma population.

Type C titanites with homogeneous age populations ranging from 113.6 to 110.4 Ma give temperatures of 765–896 °C (Table 2). Within individual samples, temperatures variations are minor and sample populations are characterized by low standard deviations ranging from 13 to 28 °C. LASS grain traverses also show no apparent temperature variation from exterior to interior domains. We do not observe any apparent correlation between temperature and geographic location. The youngest dated sample in this population, a 104.7 Ma hornblende orthogneiss from the hanging wall of the DSSZ (12NZ24), also gives the lowest temperature of 742 °C suggesting a covariation between temperature and age (see also Fig. 14A).

Type O Cretaceous titanites with dates ranging from 116.2 to 107.6 give temperatures ranging from 753 to 887 °C (Table 2). Within a single sample, multiple age populations generally yield indistinguishable temperatures; however, intrapopulation temperatures show somewhat more variability compared to type C titanites (e.g., standard deviation of temperatures in Table 2). In LASS grain traverses, a few exterior domains show statistically lower temperatures than interior domains that may be consistent with limited Zr mobility by volume diffusion (e.g., spot 13NZ54–20; see Supplemental File text). LASS grain maps (Figs. 8A–8D) reveal lower temperatures in exterior domains (~780–800 °C) compared to those in an apparent core (~820–840 °C). Integrating temperatures and $^{206}Pb/^{238}U$ dates suggests that the titanite in Figure 8 underwent incomplete and/or prolonged crystallization or recrystallization during Cretaceous metamorphism with limited evidence for diffusive reequilibration by thermally mediated volume diffusion.

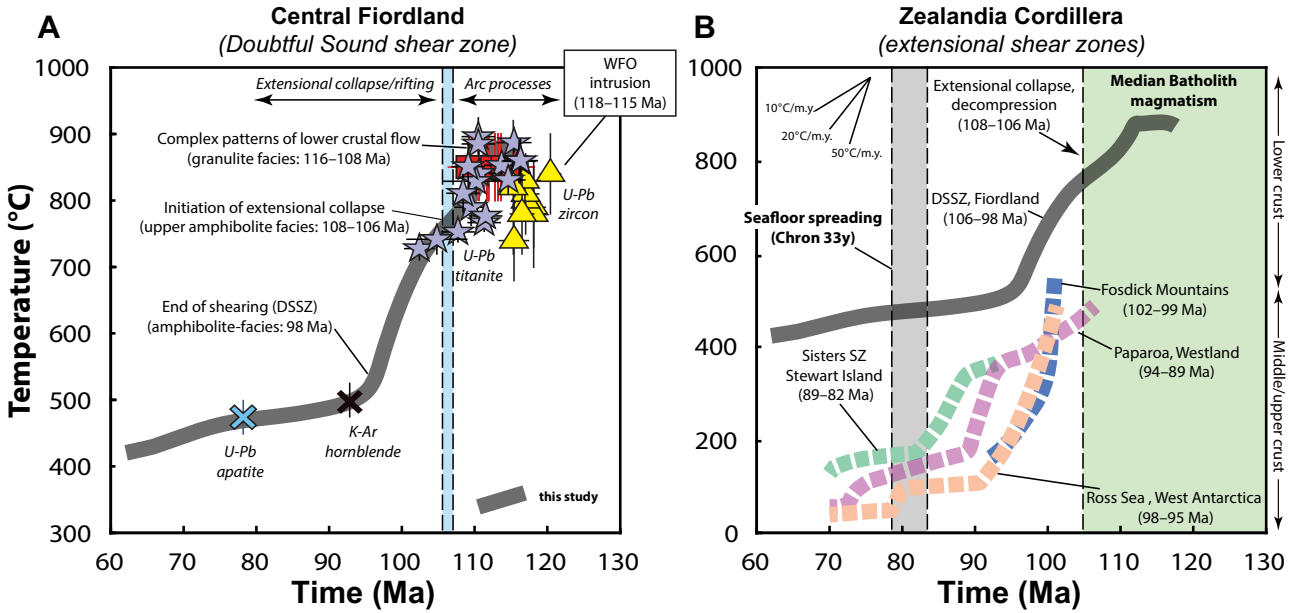

Figure 14. Time-temperature plots for extensional shear zones in the Zealandia Cordillera. (A) Data for the Doubtful Sound shear zone (DSSZ) include igneous zircon (yellow triangles; Sadorski, 2015), titanite (purple stars; this study), garnet (red squares as in Fig. 3; Stowell et al. 2014), hornblende (black x; Gibson et al., 1988), and apatite (blue x; Mattinson et al., 1986). A best-fit cooling profile is shown by gray curve. Dashed vertical lines indicate the beginning of extensional orogenic collapse 106 Ma. WFO—Western Fiordland Orthogneiss. (B) Thermal data for extensional shear zones in the Zealandia Cordillera. The timing of Median Batholith magmatism is given by green shaded area, and the timing of seafloor spreading in the Tasman Sea is shown by gray shaded box. Cooling curves show the DSSZ (this study), Fosdick Mountains (McFadden et al., 2007, 2015), Paparoa metamorphic core complex (Tulloch and Kimbrough, 1989; Spell et al. 2000), Ross Sea (Fitzgerald and Baldwin, 1997; Siddoway et al., 2004), and Sisters shear zone (Kula et al., 2007).

DISCUSSION

Our zircon and titanite data from central Fiordland allow us to clarify existing thermochronologic relationships and provide links between U-Pb chronometers and specific deformation fabrics developed in the lower crust during the transition from arc-construction to extensional orogenic collapse. Prior to this study, existing thermochronologic data yielded conflicting information regarding the initiation and cessation of lower crustal extension (see contrasting models in Fig. 3). Titanite and garnet thermochronometers, in particular, yield similar dates, but have been interpreted to record very different temperature conditions and cooling rates during the same interval of time (Flowers et al., 2005; Stowell et al., 2014). The controversy centers in part on the assumption that titanite Pb/U dates record cooling through the closure temperature of ~650–550 °C (Flowers et al., 2005). Although the use of closure temperature for titanite is commonly employed in documenting the thermal evolution of high-grade terranes, for the concept to be applied it must be demonstrated that (1) new or relict titanites were completely purged of radiogenic daughter products during the last deformational or metamorphic event, (2) titanites had a simple cooling history through the closure temperature following metamorphism, and (3) isotopic exchange of Pb during cooling was accomplished by volume diffusion (rather than a recrystallization process; Dodson, 1973).

We evaluated titanite data from central Fiordland, and show that most samples fail to meet the Dodson (1973) criteria. We caution against interpreting titanite dates as recording passage through a closure temperature and present a new thermotectonic model that documents (1) time scales and durations over which the lower crust remained thermally weakened and able to accommodate flow and (2) how rheological transitions were linked to the transient thermal structure of the lower crust during extensional orogenic collapse. We explore the significance of our thermotectonic model in light of regional extensional patterns in the greater Zealandia Cordillera.

Time Scales and Durations of Arc Root Metamorphism and Cooling

Regional-scale zircon and titanite chronology and thermometry reveal four general patterns that characterize high-*T* metamorphism in central Fiordland: (1) pre-Cretaceous, type P metamorphic titanite dates are preserved exclusively in metamorphic rocks (Deep Cove Gneiss) at the margins of the WFO or at significant structural distances away from the WFO; (2) the vast majority of Cretaceous titanite and zircon dates overlap within error and range from 116.3 to 107.6 Ma with zirconium-in-titanite temperatures ≥750 °C; (3) some Cretaceous zircon and titanite populations are characterized by an overdispersion in $^{206}Pb/^{238}U$ dates that span ~5 m.y. or more; and (4) a minor population of zircon and titanite dates range from 105.6 to 102.3 Ma and yield upper amphibolite facies temperatures of 740–730 °C. These samples are concentrated within and above the DSSZ in the Doubtful Sound region (Fig. 12). We discuss implications for these observations in the following.

Pre-Cretaceous Metamorphism

Previous geochronologic studies of zircon, titanite, garnet, and monazite in central Fiordland have documented multiple phases of pre-Cretaceous, regional high-grade metamorphism at 375–355 and 340–330 Ma (Ireland and Gibson, 1998; Flowers et al., 2005; Chavez et al., 2007; Daczko et al. 2009). Two samples from our data set (13VA178a and 12DC04e) yield significant populations of pre-Cretaceous titanite dates, and both are located either at the margins of the WFO or >500 m structurally above the WFO. Sample 13VA178a preserves the most homogeneous, pre-Cretaceous titanite population and records a temperature of ~750 °C. These results support prior field and metamorphic studies that document the preservation of Paleozoic mineral assemblages in paragneisses and calc-silicates outside of the WFO thermal aureole (Allibone et al., 2009b; Daczko et al., 2009).

Cretaceous High-T Metamorphism (116–108 Ma)

More than 90% of samples in this study yield zircon and titanite dates ranging from 116 to 108 Ma (Table 2) with corresponding zirconium-in-titanite temperatures ≥750 °C. Sparse, pre-Cretaceous titanites are preserved in only two samples, suggesting that pre-Cretaceous titanite populations were completely to nearly completely reset during Cretaceous high-*T*–high-*P* metamorphism. The oldest titanites from both type C and O subgroups and zircon cores yield dates of 116–114 Ma that overlap with the waning stages of WFO emplacement in central Fiordland from 118 to 115 Ma (Table 3; Fig. 2). Titanites in this oldest Cretaceous age range give temperatures of ~831–887 °C, indistinguishable from titanium-in-zircon temperatures from igneous zircons in the WFO (Tables 1 and 2; Fig. 14A). Metamorphic zircons in this study yield dates ranging from 116.3 to 112.3 Ma and have trace element concentrations that are distinct from those in mafic to intermediate plutonic rocks of the WFO (Fig. 11). These unique geochemical signatures indicate that zircons in extensional shear zones represent new metamorphic growth possibly resulting from dissolution-reprecipitation of older detrital grains, rather than igneous xenocrysts derived from tectonic shearing of the adjacent WFO. Moreover, the agreement in dates and temperatures between metamorphic titanites and zircons in this study versus igneous zircons from the WFO (Sadorski, 2015; Table 2) suggests that high-grade metamorphism of the prebatholithic host rocks was driven initially by advection of heat related to magmatic emplacement followed by latent heat of crystallization as the WFO cooled. Consequently, our metamorphic zircons present evidence for prograde heating related to garnet granulite facies metamorphism, rather than late-stage cooling during exhumation as predicted in some mass-balance models (Kohn et al., 2015).

Migmatitic textures and garnet granulite facies mineral assemblages in the WFO are well developed and have long been cited as evidence that high-*T*–high-*P* metamorphism continued after batholith construction (Oliver, 1977,

1980; Flowers et al., 2005; Klepeis et al., 2007; De Paoli et al., 2009; Stowell et al., 2014). Our 113–108 Ma titanite dates yield zirconium-in-titanite temperatures of ~900–750 °C that are identical to dates and temperatures from garnet chronology and thermobarometry in the region (Stowell et al., 2014). The coincidence of these dates and temperatures presents multiple lines of evidence for the persistence of granulite facies thermal conditions for >8 m.y. following batholith emplacement.

Significance of Cretaceous Titanite Overdispersion

A significant number of titanite-bearing samples in this study and Flowers et al. (2005) have $^{206}Pb/^{238}U$ dates (MSWD >> 1) that are inconsistent with a single age population (type O titanites; Figs. 7, 8, and 10J–10O). We consider two possibilities: the range in dates reflects (1) the effects of thermally activated intracrystalline volume diffusion of Pb, and/or (2) protracted crystallization or recrystallization by fluid flow, deformation, and/or metamorphic reactions. In all samples (except 14NZ13a), the titanite populations yield identical, ≥750 °C temperatures. These temperatures are higher than empirically or experimentally determined Pb-closure temperatures for titanite (Cherniak, 1993, 2010; Verts et al., 1996; Frost et al., 2001; Kohn and Corrie, 2011; Spencer et al., 2013), and might thus suggest that thermally activated Pb diffusion controlled Pb mobility.

However, closer inspection of titanite spot locations and dates reveals that many titanites do not show simple core-rim age zoning, as expected from diffusion-controlled Pb mobility (Fig. 7 and 8). For example, in 14NZ13c, dates to 122 Ma are located along exterior domains, whereas younger dates of ca. 106–105 Ma traverse exterior and interior spatial domains. Other samples also show complex relationships (Fig. 7). In sample 12DC47a, BSE images reveal a chemically distinct, ca. 111–109 Ma core surrounded by 117–111 Ma domains. In sample 13NZ54, core-rim variations in inclusion density are suggestive of multiple phases of growth and/or crystallization or recrystallization; however, both inclusion-free and inclusion-rich domains give overdispersed dates ranging from ca. 123 to 105 Ma. Although subtle matrix effects associated with sampling inclusion-rich domains might affect our dates in core domains, these effects cannot explain the broad temporal variability in inclusion-free rim domains. Initial common Pb isotopic variability during metamorphism is also not a likely explanation for the overdispersion in $^{206}Pb/^{238}U$ dates as type O titanites commonly have high radiogenic Pb/common Pb values with average intrasample $^{206}Pb/^{204}Pb$ values ranging from 23 to 2700 (Essex and Gromet, 2000). Collectively, these textures and variations in dates indicate preservation of complex growth and crystallization or recrystallization histories, and their $^{206}Pb/^{238}U$ dates cannot be attributed to thermally activated volume diffusion or simple core-rim crystallization processes. Instead, our observations are most consistent with titanite dates recording protracted growth and/or crystallization or recrystallization in response to deformation and/or metamorphic reactions during garnet granulite to upper amphibolite facies metamorphism (Verts et al., 1996; Frost et al., 2001; Kohn and Corrie, 2011; Spencer et al. 2013; Stearns et al., 2015).

Geographically Controlled Sustained Heating (106–102 Ma)

A minor population of zircon and titanite dates in the Doubtful Sound region preserves evidence for growth and/or crystallization or recrystallization from 106 to 102 Ma (Fig. 12). Zircon rims in the DSSZ record growth at 105.6 Ma (13NZ61), and 2 titanite samples in the DSSZ and in its hanging wall give dates of 104.7 and 102.3 Ma with corresponding temperatures of 742 and 728 °C, respectively (12NZ24 and 14NZ13a). The presence of young zircon and titanite dates within the DSSZ directly link growth and/or crystallization or recrystallization at 106–102 Ma to upper amphibolite facies deformation. Syntectonic dikes in the DSSZ yield dates of 102–101 Ma and further support deformation at this time (Klepeis et al., 2007, 2016).

Sample 12NZ24 is well outside the DSSZ (Fig. 2), but displays a strong amphibolite facies overprint, suggesting that the spatial footprint of upper amphibolite facies metamorphism was larger than discrete mylonitic shear zones. Allibone et al. (2009a) considered this portion of the Misty pluton as a separate magmatic phase (hornblende diorite unit: Fig. 2); however, another interpretation supported by our data and regional mapping (Rattenbury and Isaac, 2012) is that this region is a zone of widespread amphibolite facies metamorphism (see stripe and hachure patterns in Misty pluton; Fig. 2). This suggestion highlights the complexity and importance of linking zircon and titanite growth and/or crystallization or recrystallization with metamorphic fabrics in resolving disparate tectonic, magmatic, and thermal interpretations for lower crustal evolution (Allibone et al., 2009a; Rattenbury and Isaac, 2012).

Documenting the full regional extent of amphibolite facies metamorphism will require more extensive thermochronology work, particularly in eastern Fiordland. However, one unpublished titanite date in the Mount Hall region, ~14 km northeast of sample 12NZ24, yielded a date of 99 Ma and a zirconium-in-titanite temperature of 689 ± 25 °C (gray star in Fig. 12). Together with our data, these dates define an apparent geographically controlled pulse of regional, upper amphibolite facies heating from 106 to 99 Ma that extended from central Doubtful Sound to eastern Fiordland (Fig. 12). We note that this region of young dates (younger than 106 Ma; Fig. 12) is remarkably similar to the zone of widespread amphibolite facies metamorphism in the Misty pluton (Fig. 2). No plutons of this age have been identified at the current level of exposure in this region; however, postorogenic, A-type granitic dikes have dates of 105–97 Ma (Klepeis et al., 2013). The A-type character of the dikes suggests that sustained heating of the WFO was not related to continued subduction-related magmatism, but is compatible with other mechanisms such as slab breakoff, asthenospheric upwelling during the onset of extension

(Tulloch et al., 2009b), and/or foundering of a high-density arc root (Klepeis et al., 2016). Further geochemical work is needed to elucidate the origin of this apparent lower crustal thermal pulse.

Thermal Evolution of the Lower Crust During Rheological Transitions (124–90 Ma)

Our thermotectonic model that integrates field and thermochronologic results with existing structural observations (Fig. 12–14) allows us to evaluate previous interpretations (e.g., Flowers et al., 2005; Klepeis et al., 2007; Stowell et al., 2014) and improve these models in the following ways: (1) we interpret titanite dates and temperatures not as cooling ages but as recording protracted growth and/or crystallization or recrystallization in the thermal aureole of the WFO during and following emplacement; (2) zircon and titanite thermochronologic results document the persistence of granulite facies temperatures for >8 m.y. following arc flareup, during which the lower crust was thermally weakened and partially molten; and (3) we show that extensional orogenic collapse in the lower crust initiated during the interval from 108–106 Ma in the DSSZ and was associated with decompression, hydration, and a regional pulse of lower crustal heating at amphibolite facies conditions that extended beyond the footprint of extensional shear zones. In our model, we distinguish between arc-construction processes related to contractional thickening, WFO emplacement and heating, and rift-related processes that led to the opening of the Tasman Sea at 83 Ma (Fig. 14). To illustrate the transient thermal structure of the lower crust, we present a series of *t-T* slices in Figure 13. A representative *t-T* plot for the DSSZ is shown in Figure 14.

Our thermotectonic model begins with the final emplacement of the WFO during a voluminous burst of mafic to intermediate magmatism in central Fiordland (Mattinson et al., 1986; Tulloch and Kimbrough, 2003; Hollis et al., 2004; Sadorski, 2015). The main phase of magmatism and lower crustal heating in central Fiordland occurred during emplacement of the Misty and Malaspina plutons from 118 to 115 Ma (Mattinson et al., 1986; Tulloch and Kimbrough, 2003; Hollis et al., 2004; Sadorski, 2015). Igneous textures related to batholith construction reveal the development of igneous layering and emplacement-related disruption of hornblende and garnet-pyroxenite cumulates as WFO magmas were emplaced into a lower crustal MASH zone. Titanium-in-zircon temperatures for WFO magmas range from 740 to 840 °C, and these are likely minimum temperatures as zircon is a late-forming igneous phase in dioritic magmas. This stage marks the final phase of batholith construction in this sector of Zealandia, and overlapped with crustal thickening and contractional deformation in the Caswell Sound fold-thrust belt from 117 to 113 Ma (this study) and transpressional deformation in the Indecision Creek and George Sound shear zones in northern Fiordland from 119 to 111 Ma (Marcotte et al., 2005).

Accompanying final magma emplacement and crystallization was a period of sustained heating, partial melting, and lower crustal weakening at eclogite to garnet granulite facies conditions, which lasted at least 8 m.y. from 116 to 108 Ma (Figs. 13 and 14). High temperatures (>750 °C) in footwall, shear zone, and hanging-wall rocks of the DSSZ and RISZ were provided by latent heat of crystallization in the WFO with possible additions from underplated A-type magmas related to felsic dikes. Paleozoic titanites in prebatholithic host rocks within the thermal aureole of the WFO were completely recrystallized and reset during prograde metamorphism (Table 2). Metamorphic zircons also developed during this time and capture the timing of prograde metamorphism in the arc root. High temperatures led to the development of garnet- and clinopyroxene-rich granulitic assemblages and local migmatization of the WFO and host rocks.

Following this interval of high-*T* heating, a tectonic break occurred at 108–106 Ma and was associated with cooling from garnet granulite to upper amphibolite facies conditions, decompression, hydration, and the initiation of extensional orogenic collapse (Klepeis et al., 2007) (Fig. 14A). In both the RISZ and DSSZ, upper amphibolite facies fabrics record progressive strain focusing and subhorizontal flow along arrays of mylonitic shear zones that facilitated crustal thinning and decompression (Klepeis et al., 2007). Our zircon and titanite dates from these shear zones record new growth and/or crystallization or recrystallization during this interval that are compatible with a period of sustained heating >700 °C from 106 to 102 Ma in the DSSZ region. Our RISZ footwall sample, 12NZ07, yielded the youngest titanite date in this study (95.2 ± 8.9 Ma) and may record diachronous heating in the Breaksea region.

Spatiotemporal patterns in our data suggest that upper amphibolite facies heating from ca. 106 to 99 Ma was geographically concentrated and/or sustained in the DSSZ and in its hanging wall, extending from the southeastern Misty pluton to eastern Fiordland (Figs. 12 and 13). This apparent geographic footprint likely reflects deep-seated heating related to continued A-type diking in the region. In Tulloch et al. (2009b) it was speculated that ca. 101–97 Ma A-type tuffs located throughout Zealandia may reflect the onset of rifting of Zealandia from West Antarctica. The A-type dikes and the spatiotemporal pattern we observe in Fiordland may reflect this same lithospheric thinning. An alternative, although not mutually exclusive, possibility is that foundering of a high-density arc root formed from magmatic crystallization of high-*P* garnet pyroxenite may have initiated asthenospheric upwelling beneath central Fiordland and driven lower crustal thinning. Structural studies in the Breaksea region document vertical flow of gneiss domes in response to density contrasts between garnet pyroxenites and melt-rich granulites (Betka and Klepeis, 2013; Klepeis et al., 2016). Numerical models of arc root foundering predict time scales of ~10 m.y. or more following crystallization, consistent with the time scales of arc root heating after WFO emplacement in the Breaksea area (Jull and Kelemen, 2001; Dufek and Bergantz, 2005; Lee, 2014).

The high temperatures (>700 °C) we document in hanging-wall and shear zone rocks also have implications for the relationship between WFO and wall rocks, and postulated large-magnitude vertical displacements. Our temperature data from within shear zone and hanging-wall rocks record granulite facies temperatures that overlap with zircon crystallization temperatures from adjacent footwall rocks (Tables 2 and 3). These results confirm that portions of the Deep Cove Gneiss were located within the thermal aureole of the WFO

during magmatic emplacement and underwent cooling from garnet granulite to upper amphibolite facies conditions during progressive strain localization (Allibone et al., 2009b; Daczko et al., 2009). Least squares regression of titanite temperatures and dates gives a regional cooling rate of 13.5 ± 6.8 °C/m.y. over the temperature range of 900–700 °C. For the DSSZ only, the rate is 8.3 ± 6.6 °C/m.y. (Fig. 12, inset; Fig. 14). Although these rates have large uncertainties, they are ~2–4× slower than rates estimated by Flowers et al. (2005) based on assumed zircon and titanite closure temperatures. Our data thus demonstrate that the lower crust remained hot and weak for at least 8 m.y. during the rheological transition from granulite facies lower crustal flow to extensional orogenic collapse.

Patterns of Regional Extension in Zealandia

Our data from central Fiordland document a prolonged (>8 m.y.) granulite facies thermal pulse that resulted in the lower crust remaining hot (>750 °C) and weak from 116 to 108 Ma. Contractional deformation and crustal thickening recorded in the Caswell fold-thrust belt ceased during this interval and were followed by complex patterns of lower crustal flow involving both vertical and horizontal displacements (Klepeis et al., 2007, 2016; Betka and Klepeis, 2013). Garnet granulite facies metamorphism, partial melting, and lower crustal flow processes occurred at largely isobaric conditions and were not accompanied by decompression (Stowell et al., 2014). However, by 108–106 Ma, orogenic collapse was underway in the lower crust of the Median Batholith and marked the beginning of extension and decompression (Klepeis et al., 2007) leading to rifting and continental break-up throughout Zealandia (Bradshaw, 1989b; Mortimer, 2008). Data from other parts of the Median Batholith reveal that final high Sr/Y (possibly subduction related) magmatism occurred at 105 Ma (Tulloch and Kimbrough, 2003; green field in Fig. 14B). Subsequent A-type magmatism from 101 to 97 Ma occurred throughout the width of Zealandia and has been interpreted to signify extension within the orogen as a consequence of plate reorganization (Tulloch et al., 2009b).

Kula et al. (2007) proposed a two phase model for continental breakup of Zealandia that involved (1) northward propagation of the Tasman ridge between Zealandia and West Antarctica and East Antarctica and Australia from 101 to 88 Ma; and (2) opening of the Pacific-Antarctic spreading ridge between Zealandia and West Antarctica at 89–82 Ma (Fig. 1; Kula et al. 2007). Regional extensional features related to their initial stage include oblique detachment structures in the Fosdick Mountains, Antarctica, at 102–99 Ma (McFadden et al., 2007, 2015), detachment structures in the Ross Sea at 98–95 (Fitzgerald and Baldwin, 1997; Siddoway et al., 2004), and core complexes in upper to mid-crustal rocks in Westland, South Island, New Zealand, at 94–89 Ma (Tulloch and Kimbrough, 1989; Spell et al., 2000). The second phase of continental breakup is manifested by detachment structures in the Sisters shear zone, Stewart Island, New Zealand, at 89–82 Ma (Kula et al., 2007; Ring et al., 2015), and seafloor spreading in the Tasman Sea at 83 Ma and the Pacific-Antarctic spreading ridge at 79 Ma (Fig. 1; Stock and Cande, 2002).

Our dates from central Fiordland suggest that extensional structures in the lower crust developed even earlier than proposed in the Kula et al. (2007) model and marked the development of organized networks of upper amphibolite facies shear zones from 108 to 106 Ma as batholithic construction and garnet granulite facies heating ceased (Fig. 14B). We postulate that the prolonged period (>15 m.y.) of lower crustal heating resulted in rheological weakening of the arc root and was a key factor in controlling the transition from crustal thickening to crustal thinning and extensional orogenic collapse.

CONCLUSIONS

The thermochronology of metamorphic zircon and titanite from the lower crust of central Fiordland captures the timing of both prograde granulite facies metamorphism and crystal-plastic flow from 116 to 108 Ma, and subsequent retrograde amphibolite facies metamorphism in high-strain zones from 106 to 102 Ma. Titanite LASS analysis reveals that most samples display an overdispersion of dates (>5–10 m.y.) that cannot be explained by volume diffusion or simple, monotonic cooling through a closure temperature following metamorphism. Instead, we interpret titanite dates as reflecting protracted crystallization or recrystallization and/or growth over ~15 m.y. during the transition from granulite to amphibolite facies conditions. Our observations require reevaluation of previous thermotectonic models for the lower crust based on assumed titanite closure temperatures.

Our results are incorporated into a thermotectonic model that involves (1) thermal weakening of the lower crust during a short-lived burst of mafic to intermediate magmatism from 118 to 115 Ma that coincided with crustal thickening and contractional deformation in the Caswell Sound fold-thrust belt; (2) protracted, eclogite to garnet granulite facies metamorphism, partial melting, and lower crustal flow over ~8 m.y. from 116 to 108 Ma; and (3) localization of extensional strain in upper amphibolite facies shear zones accompanied by decompression and hydration starting at 108–106 Ma in the DSSZ. Our results demonstrate that the lower crust in central Fiordland remained hot (>750 °C), partially molten, and thermally weakened for longer than previously proposed (Flowers et al., 2005; Klepeis et al., 2007), and facilitated the initial tectonic transition from crustal thickening to extensional collapse of the Zealandia Cordillera within the Fiordland sector of the Median Batholith during the interval 108 to 106 Ma. The rheological transition from complex horizontal and vertical flow at granulite facies to organized shearing in upper amphibolite facies mylonite zones resulted from the decay of thermal energy after arc flareup as viscosity of the lower crust increased. We observe that sustained upper amphibolite facies heating extended beyond the footprint of extensional shear zones and reflects the presence of transient lower crustal thermal anomalies resulting from lithospheric thinning and asthenospheric upwelling. We propose that orogenic collapse of the Zealandia Cordillera in the lower crust of the Median Batholith initiated as a direct consequence of prolonged (>15 m.y.) thermal weakening of the lower arc crust.

ACKNOWLEDGMENTS

We thank Art Snoke for sharing his encyclopedic knowledge and enthusiasm for geology with many budding geologists over the years (including Stowell and Schwartz). We acknowledge stimulating discussions with Nick Mortimer, Mike Palin, Nathan Daczko, and Robinson Cecil. Reviews by editor Shan de Silva, associate editor Al McGrew, Cam Davidson, and two anonymous reviewers significantly improved our manuscript. We thank Brad Ito for keeping the SHRIMP-RG (sensitive high-resolution ion microprobe–reverse geometry) working well and efficiently, Carol Zamora for assistance with zircon geochronology, and Brian Clements for assistance with modeling shown in Figure 13. Financial support for this work was provided by National Science Foundation grants EAR-1352021 (Schwartz), EAR-1119039 (Stowell and Schwartz), and EAR-1119248 (Klepeis).

REFERENCES CITED

Allibone, A.H., Jongens, R., Turnbull, I.M., Milan, L.A., Daczko, N.R., DePaoli, M.C., and Tulloch, A.J., 2009a, Plutonic rocks of Western Fiordland, New Zealand: Field relations, geochemistry, correlation, and nomenclature: New Zealand Journal of Geology and Geophysics, v. 52, p. 379–415, doi:10.1080/00288306.2009.9518465.

Allibone, A.H., Milan, L.A., Daczko, N.R., and Turnbull, I.M., 2009b, Granulite facies thermal aureoles and metastable amphibolite facies assemblages adjacent to the Western Fiordland Orthogneiss in southwest Fiordland, New Zealand: Journal of Metamorphic Geology, v. 27, p. 349–369, doi:10.1111/j.1525-1314.2009.00822.x.

Behn, M.D., Lin, J., and Zuber, M.T., 2002, A continuum mechanics model for normal faulting using a strain-rate softening rheology: Implications for thermal and rheological controls on continental and oceanic rifting: Earth and Planetary Science Letters, v. 202, p. 725–740, doi: 10.1016/S0012-821X(02)00792-6.

Betka, P.M., and Klepeis, K.A., 2013, Three-stage evolution of lower crustal gneiss domes at Breaksea entrance, Fiordland, New Zealand: Tectonics, v. 32, p. 1084–1106, doi:10.1002/tect.20068.

Bolhar, R., Weaver, S.D., Palin, J.M., Cole, J.W., and Paterson, L.A., 2008, Systematics of zircon crystallisation in the Cretaceous Separation Point Suite, New Zealand, using U/Pb isotopes, REE and Ti geothermometry: Contributions to Mineralogy and Petrology, v. 156, p. 133–160, doi:10.1007/s00410-007-0278-5.

Bonamici, C.E., Kozdon, R., Ushikubo, T., and Valley, J.W., 2014, Intragrain oxygen isotope zoning in titanite by SIMS: Cooling rates and fluid infiltration along the Carthage-Colton Mylonite Zone, Adirondack Mountains, NY, USA: Journal of Metamorphic Geology, v. 32, p. 71–92, doi:10.1111/jmg.12059.

Bradshaw, J.Y., 1989a, Early Cretaceous vein-related garnet granulite in Fiordland, southwest New Zealand: A case for infiltration of mantle-derived CO_2-rich fluids: Journal of Geology, v. 97, p. 697–717, doi:10.1086/629353.

Bradshaw, J.Y., 1989b, Origin and metamorphic history of an Early Cretaceous polybaric granulite terrain, Fiordland, southwest New Zealand: Contributions to Mineralogy and Petrology, v. 103, p. 346–360, doi:10.1007/BF00402921.

Brown, E., 1996, High-pressure metamorphism caused by magma loading in Fiordland, New Zealand: Journal of Metamorphic Geology, v. 14, p. 441–452, doi:10.1046/j.1525-1314.1996.06024.x.

Buck, W.R., 1991, Modes of continental lithospheric extension: Journal of Geophysical Research, v. 96, p. 20,161–20,178, doi:10.1029/91JB01485.

Chambers, J.M., and Kohn, M.J., 2012, Titanium in muscovite, biotite, and hornblende: Modeling, thermometry, and rutile activities of metapelites and amphibolites: American Mineralogist v. 97, p. 543–555.

Chavez, T., Grace, R., and Stowell, H.H., 2007, New garnet Sm-Nd evidence for Paleozoic metamorphism, Wet Jacket Arm Fiordland, New Zealand: Geological Society of America Abstracts with Programs, v. 39, no. 4, p. 145–155.

Cherniak, D.J., 1993, Lead diffusion in titanite and preliminary results on the effects of radiation damage on Pb transport: Chemical Geology, v. 110, p. 177–194, doi:10.1016/0009-2541(93)90253-F.

Cherniak, D.J., 2006, Zr diffusion in titanite: Contributions to Mineralogy and Petrology, v. 152, p. 639–647, doi: 10.1007/s00410-006-0133-0.

Cherniak, D.J., 2010, Diffusion in accessory minerals: Zircon, titanite, apatite, monazite and xenotime: Reviews in Mineralogy and Geochemistry, v. 72, p. 827–869, doi:10.2138/rmg.2010.72.18.

Cherniak, D.J., and Watson, E.B., 2001, Pb diffusion in zircon: Chemical Geology, v. 172, p. 5–24, doi:10.1016/S0009-2541(00)00233-3.

Clarke, C.L., Klepeis, K.A., and Daczko, N.R., 2000, Cretaceous high-P granulites at Milford Sound, New Zealand: Metamorphic history and emplacement in a convergent margin setting: Journal of Metamorphic Geology, v. 18, p. 359–374, doi:10.1046/j.1525-1314.2000.00259.x.

Clarke, G.L., Daczko, N.R., and Miescher, D., 2013, Identifying relic igneous garnet and clinopyroxene in eclogite and granulite, Breaksea orthogneiss, New Zealand: Journal of Petrology, v. 54, p. 1921–1938, doi: 10.1093/petrology/egt036.

Clements, B.L., Schwartz, J.J., Stowell, H.H., Klepeis, K.A., Kylander-Clark, A., Hacker, B., and Tulloch, A., 2014, Punctuated cooling of an arc root during extensional orogenic collapse, central Fiordland, New Zealand: Integrating zircon, titanite and rutile thermochronology: Geological Society of America Abstracts with Programs, v. 46, no. 6, p. 157.

Cooper, R., and Tulloch, A., 1992, Early Palaeozoic terranes in New Zealand and their relationship to the Lachlan Fold Belt: Tectonophysics, v. 214, p. 129–144, doi:10.1016/0040-1951(92)90193-A.

Daczko, N.R., Klepeis, K.A., and Clarke, G.L., 2001, Evidence of early Cretaceous collisional-style orogenesis in Northern Fiordland, New Zealand and its effects on the evolution of the lower crust: Journal of Structural Geology, v. 23, p. 693–713, doi: 10.1016/S0191-8141(00)00130-9.

Daczko, N.R., Klepeis, K.A., and Clarke, G.L., 2002, Thermomechanical evolution of the crust during convergence and deep crustal pluton emplacement in the Western Province of Fiordland, New Zealand: Tectonics, v. 21, doi: 10.1029/2001TC001282.

Daczko, N.R., Milan, L.A., and Halpin, J.A., 2009, Metastable persistence of pelitic metamorphic assemblages at the root of a Cretaceous magmatic arc—Fiordland, New Zealand: Journal of Metamorphic Geology, v. 27, p. 233–247, doi: 10.1111/j.1525-1314.2009.00815.x.

De Paoli, M.C., Clarke, G.L., Klepeis, K.A., Allibone, A.H., and Turnbull, I.M., 2009, The eclogite-granulite transition: Mafic and intermediate assemblages at Breaksea sound, New Zealand: Journal of Petrology, v. 50, p. 2307–2343, doi:10.1093/petrology/egp078.

Dewey, J.F., 1988, Extensional collapse of orogens: Tectonics, v. 7, 1123, doi:10.1029/TC007i006p01123.

Dodson, M.H., 1973, Closure temperature in cooling geochronological and petrological systems: Contributions to Mineralogy and Petrology, v. 40, p. 259–274, doi:10.1007/BF00373790.

Dufek, J., and Bergantz, G.W., 2005, Lower crustal magma genesis and preservation: A stochastic framework for the evaluation of basalt-crust interaction: Journal of Petrology, v. 46, p. 2167–2195, doi:10.1093/petrology/egi049.

Essex, R.M., and Gromet, L.P., 2000, U-Pb dating of prograde and retrograde titanite growth during the Scandian orogeny: Geology, v. 28, p. 419–422, doi:10.1130/0091-7613(2000)28<419:UDOPAR>2.0.CO;2.

Fitzgerald, P.G., and Baldwin, S.L., 1997, Detachment fault model for the evolution of the Ross Embayment, *in* Ricci C.A., ed., The Antarctic region: Geological evolution and processes: Siena, Terra Antartica, p. 555–564.

Flowers, R.M., Bowring, S., Tulloch, A.J., and Klepeis, K.A., 2005, Tempo of burial and exhumation within the deep roots of a magmatic arc, Fiordland, New Zealand: Geology, v. 33, p. 17–20, doi:10.1130/G21010.1.

Foster, D.A., and Gray, D.R., 2000, Evolution and structure of the Lachlan Fold Belt (orogen) of eastern Australia: Annual Review of Earth and Planetary Sciences, v. 28, p. 47–80, doi:10.1146/annurev.earth.28.1.47.

Franz, G., and Spear, F.S., 1985, Aluminous titanite (sphene) from the eclogite zone, south-central Tauern Window, Austria: Chemical Geology, v. 50, p. 33–46, doi:10.1016/0009-2541(85)90110-X.

Frost, B.R., Chamberlain, K.R., and Schumacher, J.C., 2001, Sphene (titanite): Phase relations and role as a geochronometer: Chemical Geology, v. 172, p. 131–148, doi:10.1016/S0009-2541(00)00240-0.

Gaina, C., Müller, D.R., Royer, J.-Y., Stock, J., Hardebeck, J., and Symonds, P., 1998, The tectonic history of the Tasman Sea: A puzzle with 13 pieces: Journal of Geophysical Research, v. 103, p. 12,413–12,433, doi:10.1029/98JB00386.

Gascoyne, M., 1986, Evidence for the stability of the potential nuclear waste host, sphene, over geological time, from uranium-lead ages and uranium-series measurements: Applied Geochemistry, v. 1, p. 199–210, doi:10.1016/0883-2927(86)90004-1.

Gibson, G.M., 1992, Medium-high-pressure metamorphic rocks of the Tuhua Orogen, western New Zealand, as lower crustal analogues of the Lachlan Fold Belt, SE Australia: Tectonophysics, v. 214, p. 145–157, doi:10.1016/0040-1951(92)90194-B.

Gibson, G.M., and Ireland, T.R., 1995, Granulite formation during continental extension in Fiordland, New Zealand: Nature, v. 375, p. 479–482, doi:10.1038/375479a0.

Gibson, G.M., McDougall, I., and Ireland, T.R., 1988, Age constraints on metamorphism and the development of a metamorphic core complex in Fiordland, southern New Zealand: Geology, v. 16, p. 405–408, doi:10.1130/0091-7613(1988)016<0405:ACOMAT>2.3.CO;2.

Gibson, G.M., and Ireland, T.R., 1996, Extension of Delamerian (Ross) orogen into western New Zealand: Evidence from zircon ages and implications for crustal growth along the Pacific margin of Gondwana: Geology, v. 24, p. 1087–1090, doi:10.1130/0091-7613(1996)024<1087:EODROI>2.3.CO;2.

Hanson, G.N., Catanzaro, E.J., and Anderson, D.H., 1971, U-Pb ages for sphene in a contact metamorphic zone: Earth and Planetary Science Letters, v. 12, p. 231–237, doi:10.1016/0012-821X(71)90082-3.

Hayden, L.A., Watson, E.B., and Wark, D.A., 2008, A thermobarometer for sphene (titanite): Contributions to Mineralogy and Petrology, v. 155, p. 529–540, doi:10.1007/s00410-007-0256-y.

Hollis, J.A., Clarke, G.L., Klepeis, K.A., Daczko, N.R., and Ireland, T.R., 2003, Geochronology and geochemistry of high-pressure granulites of the Arthur River Complex, Fiordland, New Zealand: Cretaceous magmatism and metamorphism on the palaeo-Pacific Margin: Journal of Metamorphic Geology, v. 21, p. 299–313, doi:10.1046/j.1525-1314.2003.00443.x.

Hollis, J.A., Clarke, G.L., Klepeis, K.A., Daczko, N.R., and Ireland, T.R., 2004, The regional significance of Cretaceous magmatism and metamorphism in Fiordland, New Zealand, from U-Pb zircon geochronology: Journal of Metamorphic Geology, v. 22, p. 607–627, doi:10.1111/j.1525-1314.2004.00537.x.

Hopper, J.R., and Buck, W.R., 1998, Styles of extensional decoupling: Geology, v. 26, p. 699–702, doi:10.1130/0091-7613(1998)026<0699:SOED>2.3.CO;2.

Hout, C., Stowell, H.H., Schwartz, J.J., and Klepeis, K., 2012, New $^{206}Pb/^{238}U$ zircon ages record magmatism and metamorphism in the crustal root of a magmatic arc, Fiordland, New Zealand: Geological Society of America Abstracts with Programs, v. 44, no. 7, p. 586.

House, M.A., Gurnis, M., Sutherland, R., and Kamp, P.J.J., 2005, Patterns of Late Cenozoic exhumation deduced from apatite and zircon U-He ages from Fiordland, New Zealand: Geochemistry, Geophysics, Geosystems, v. 6, doi: 10.1029/2005GC000968.

Hout, C., Stowell, H.H., Schwartz, J.J., and Klepeis, K., 2013, New garnet Sm-Nd ages record timing of eclogitic garnet growth in Fiordland, New Zealand: Geological Society of America Abstracts with Programs, v. 45, no. 7, p. 799.

Huismans, R.S., Buiter, S.J.H., and Beaumont, C., 2005, Effect of plastic-viscous layering and strain softening on mode selection during lithospheric extension: Journal of Geophysical Research, v. 110, B02406, doi:10.1029/2004JB003114.

Ireland, T.R., and Gibson, G.M., 1998, SHRIMP monazite and zircon geochronology of high-grade metamorphism in New Zealand: Journal of Metamorphic Geology, v. 16, p. 149–167, doi:10.1111/j.1525-1314.1998.00112.x.

Jull, M., and Kelemen, P.B., 2001, On the conditions for lower crustal convective instability: Journal of Geophysical Research, v. 106, p. 6423–6446, doi:10.1029/2000JB900357.

Kapp, P., Taylor, M., Stockli, D., and Ding, L., 2008, Development of active low-angle normal fault systems during orogenic collapse: Insight from Tibet: Geology, v. 36, p. 7–10, doi:10.1130/G24054A.1.

Kimbrough, D.L., Tulloch, A.J., Geary, E., Coombs, D.S., and Landis, C.A., 1993, Isotopic ages from the Nelson region of South Island New Zealand: Crustal structure and definition of the Median Tectonic Zone: Tectonophysics, v. 225, p. 433–448, doi:10.1016/0040-1951(93)90308-7.

Kimbrough, D.L., Tulloch, A.J., Coombs, D.S., Landis, C.A., Johnston, M.R., and Mattinson, J.M., 1994, Uranium-lead zircon ages from the Median Tectonic Zone, New Zealand: New Zealand Journal of Geology and Geophysics, v. 37, p. 393–419, doi:10.1080/00288306.1994.9514630.

Klepeis, K.A., and King, D.S., 2009, Evolution of the middle and lower crust during the transition from contraction to extension in Fiordland, New Zealand: Geological Society of America Bulletin, v. 456, p. 243–265, doi:10.1130/2009.2456(09).

Klepeis, K.A., Daczko, N.R., and Clarke, G.L., 1999, Kinematic vorticity and tectonic significance of superposed mylonites in a major lower crustal shear zone, northern Fiordland, New Zealand: Journal of Structural Geology, v. 21, p. 1385–1405, doi:10.1016/S0191-8141(99)00091-7.

Klepeis, K.A., Clarke, G.L., and Rushmer, T., 2003, Magma transport and coupling between deformation and magmatism in the continental lithosphere: GSA Today, v. 13, p. 4–11, doi:10.1130/1052-5173(2003)013<0004:MTACBD>2.0.CO;2.

Klepeis, K.A., Clarke, G.L., Gehrels, G., and Vervoort, J., 2004, Processes controlling vertical coupling and decoupling between the upper and lower crust of orogens: Results from Fiordland, New Zealand: Journal of Structural Geology, v. 26, p. 765–791, doi:10.1016/j.jsg.2003.08.012.

Klepeis, K.A., King, D., De Paoli, M., Clarke, G.L., and Gehrels, G., 2007, Interaction of strong lower and weak middle crust during lithospheric extension in western New Zealand: Tectonics, v. 26, TC401, doi:10.1029/2006TC002003.

Klepeis, K.A., Newman, A., Dianska, K.E., Schwartz, J.J., Stowell, H.H., and Tulloch, A.J., 2013, Time-scales of magmatism, metamorphism and deformation during the initiation of intraplate rifting in the lower crust of a continental arc, Fiordland, New Zealand: Geological Society of America Abstracts with Programs, v. 45, no. 7, p. 812.

Klepeis, K.A., Schwartz, J.J., Stowell, H.H., and Tulloch, A., 2016, Gneiss domes, vertical and horizontal mass transfer, and the initiation of extension in the hot lower crustal root of a continental arc, Fiordland, New Zealand: Lithosphere, doi:10.1130/L490.1.

Kohn, M.J., and Corrie, S.L., 2011, Preserved Zr-temperatures and U-Pb ages in high-grade metamorphic titanite: Evidence for a static hot channel in the Himalayan orogen: Earth and Planetary Science Letters, v. 311, p. 136–143, doi:10.1016/j.epsl.2011.09.008.

Kohn, M.J., Corrie, S.L., and Markley, C., 2015, The fall and rise of metamorphic zircon: American Mineralogist, v. 100, p. 897–908, doi: 10.2138/am-2015-5064.

Kula, J., Tulloch, A., Spell, T.L., and Wells, M.L., 2007, Two-stage rifting of Zealandia-Australia-Antarctica: Evidence from $^{40}Ar/^{39}Ar$ thermochronometry of the Sisters shear zone Stewart Island, New Zealand: Geology, v. 35, p. 411–414, doi:10.1130/G23432A.1.

Kylander-Clark, A.R.C., Hacker, B.R., and Cottle, J.M., 2013, Laser-ablation split-stream ICP petrochronology: Chemical Geology, v. 345, p. 99–112, doi:10.1016/j.chemgeo.2013.02.019.

Lavier, L.L., and Manatschal, G., 2006, A mechanism to thin the continental lithosphere at magma-poor margins: Nature, v. 440, p. 324–328, doi:10.1038/nature04608.

Lavier, L.L., Buck, W.R., and Poliakov, A.N.B., 2000, Factors controlling normal fault offset in an ideal brittle layer: Journal of Geophysical Research, v. 105, p. 23,431–23,442, doi:10.1029/2000JB900108.

Lee, C.-T.A., 2014, Physics and chemistry of deep continental crust recycling, *in* Rudnick, R., ed., The Crust: Treatise on Geochemistry 4: Amsterdam, Elsevier, p. 423–456, doi:10.1016/B978-0-08-095975-7.00314-4.

Ludwig, K.R., 2012, Isoplot 3.75, a geochronological toolkit for Excel: Berkeley Geochronology Center Special Publication 5, 75 p.

Marcotte, S.B., Klepeis, K., Clarke, G.L., Gehrels, G., and Hollis, J.A., 2005, Intra-arc transpression in the lower crust and its relationship to magmatism in a Mesozoic magmatic arc: Tectonophysics, v. 407, p. 135–163, doi:10.1016/j.tecto.2005.07.007.

Mattinson, J.M., Kimbrough, D.L., and Bradshaw, J.Y., 1986, Western Fiordland orthogneiss: Early Cretaceous arc magmatism and granulite facies metamorphism, New Zealand: Contributions to Mineralogy and Petrology, v. 92, p. 383–392, doi:10.1007/BF00572167.

McFadden, R., Siddoway, C.S., Teyssier, C., Fanning, C.M., and Kruckenberg, S.C., 2007, Cretaceous oblique detachment tectonics in the Fosdick Mountains, Marie Byrd Land, Antarctica: U.S. Geological Survey Open-File Report 2007-1047-SRP-046, doi:10.3133/ofr20071047SRP046.

McFadden, R.R., Teyssier, C., Siddoway, C.S., Cosca, M.A., and Fanning, C.M., 2015, Mid-Cretaceous oblique rifting of West Antarctica: Emplacement and rapid cooling of the Fosdick Mountains migmatite-cored gneiss dome: Lithos, v. 232, p. 306–318, doi:10.1016/j.lithos.2015.07.005.

Mortimer, N., 2004, New Zealand's geological foundations: Gondwana Research, v. 7, p. 261–272, doi:10.1016/S1342-937X(05)70324-5.

Mortimer, N., 2008, Zealandia, *in* Spencer, J.E., and Titley, S.R., eds., Ores and orogenesis: Circum-Pacific tectonics, geologic evolution, and ore deposits: Arizona Geological Society Digest 22, p. 227–233.

Mortimer, N., Tulloch, A.J., Spark, R.N., Walker, N.W., Ladley, E., Allibone, A.H., and Kimbrough, D.L., 1999, Overview of the Median Batholith, New Zealand: A new interpretation of the geology of the Median Tectonic Zone and adjacent rocks: Journal of African Earth Sciences, v. 29, p. 257–268, doi:10.1016/S0899-5362(99)00095-0.

Oliver, G.J.H., 1977, Feldspathic hornblende and garnet granulites and associated anorthosite pegmatites from Doubtful Sound, Fiordland, New Zealand: Contributions to Mineralogy and Petrology, v. 65, p. 111–121, doi:10.1007/BF00371051.

Oliver, G.J.H., 1980, Geology of the granulite and amphibolite facies gneisses of Doubtful Sound, Fiordland, New Zealand: New Zealand Journal of Geology and Geophysics, v. 23, p. 27–41, doi:10.1080/00288306.1980.10424190.

Oliver, G.J.H., 1990, An exposed cross-section of continental crust, Doubtful Sound Fiordland, New Zealand; Geophysical & Geological Setting, *in* Salisbury, M.H., and Fountain, D.M., eds., Exposed cross-sections of the continental crust: NATO ASI Series Volume 317: Dordrecht, Kluwer Academic Publishers, p. 43–69.

Platt, J.P., Behr, W.M., and Cooper, F.J., 2014, Metamorphic core complexes: Windows into the mechanics and rheology of the crust: Journal of the Geological Society [London], v. 172, p. 9–27, doi:10.1144/jgs2014-036.

Rattenbury, M., and Isaac, M., 2012, The QMAP 1:250 000 Geological Map of New Zealand project: New Zealand Journal of Geology and Geophysics, v. 55, p. 393–405, doi:10.1080/00288306.2012.725417.

Rey, P.F., and Müller, R.D., 2010, Fragmentation of active continental plate margins owing to the buoyancy of the mantle wedge: Nature Geoscience, v. 3, p. 257–261, doi:10.1038/ngeo825.

Rey, P.F., Teyssier, C., and Whitney, D.L., 2009, Extension rates, crustal melting, and core complex dynamics: Geology, v. 37, p. 391–394, doi:10.1130/G25460A.1.

Rey, P.F., Vanderhaeghe, O., and Teyssier, C., 2001, Gravitational collapse of the continental crust: Definition, regimes and modes: Tectonophysics, v. 342, p. 435–449, doi:10.1016/S0040-1951(01)00174-3.

Ring, U., Bernet, M., and Tulloch, A., 2015, Kinematic, finite strain and vorticity analysis of the Sisters shear zone, Stewart Island, New Zealand: Journal of Structural Geology, v. 73, p. 114–129, doi:10.1016/j.jsg.2015.02.004.

Sadorski, J., 2015, Time scales of continental arc root construction and deep crustal magmatic flux rates: Insights from U-Pb zircon geochronology of a Triassic–Cretaceous arc, Fiordland, New Zealand [M.S. thesis]: Northridge, California State University, 372 p.

Sambridge, M.S., and Compston, W., 1994, Mixture modeling of multi-component data sets with application to ion-probe zircon ages: Earth and Planetary Science Letters, v. 128, p. 373–390, doi:10.1016/0012-821X(94)90157-0.

Scott, D.J., and St-Onge, M.R., 1995, Constraints on Pb closure temperature in titanite based on rocks from the Ungava orogen, Canada: Implications for U-Pb geochronology and P-T-t path determinations: Geology, v. 23, p. 1123–1126, doi:10.1130/0091-7613(1995)023<1123:COPCTI>2.3.CO;2.

Siddoway, C.S., Baldwin, S.L., Fitzgerald, P.G., Fanning, C.M., and Luyendyk, B.P., 2004, Ross Sea mylonites and the timing of intracontinental extension within the West Antarctic rift system: Geology, v. 32, p. 57–60, doi:10.1130/G20005.1.

Spell, T.L., McDougall, I., and Tulloch, A.J., 2000, Thermochronologic constraints on the breakup of the Pacific Gondwana margin: The Paparoa metamorphic core complex, South Island, New Zealand: Tectonics, v. 19, p. 433–451, doi:10.1029/1999TC900046.

Spencer, K.J., Hacker, B.R., Kylander-Clark, A.R.C., Andersen, T.B., Cottle, J.M., Stearns, M.A., Poletti, J.E., and Seward, G.G.E., 2013, Campaign-style titanite U-Pb dating by laser-ablation ICP: Implications for crustal flow, phase transformations and titanite closure: Chemical Geology, v. 341, p. 84–101, doi:10.1016/j.chemgeo.2012.11.012.

Stearns, M.A., Hacker, B.R., Ratschbacher, L., Rutte, D., and Kylander-Clark, A.R.C., 2015, Titanite petrochronology of the Pamir gneiss domes: Implications for mid-deep crust exhumation and titanite closure to Pb and Zr diffusion: Tectonics, v. 34, doi:10.1002/2014TC003774.

Stock, J.M., and Cande, S.C., 2002, Tectonic history of Antarctic seafloor in the Australia–New Zealand–South Pacific sector: Implications for Antarctic continental tectonics, *in* Gamble, J.A., et al., eds., Antarctica at the close of a millennium: Royal Society of New Zealand Bulletin Volume 35, p. 251–259.

Stowell, H.H., Tulloch, A., Zuluaga, C., and Koenig, A., 2010, Timing and duration of garnet granulite metamorphism in magmatic arc crust, Fiordland, New Zealand: Chemical Geology, v. 273, p. 91–110, doi:10.1016/j.chemgeo.2010.02.015.

Stowell, H., Parker, K.O., Gatewood, M., Tulloch, A.J., and Koenig, A., 2014, Temporal links between pluton emplacement, garnet granulite metamorphism, partial melting and extensional collapse in the lower crust of a Cretaceous magmatic arc, Fiordland, New Zealand: Journal of Metamorphic Geology, v. 32, p. 151–175, doi:10.1111/jmg.12064.

Tucker, R.D., Råheim, A., Krogh, T.E., and Corfu, F., 1987, Uranium-lead zircon and titanite ages from the northern portion of the Western Gneiss region, south-central Norway: Earth and Planetary Science Letters, v. 81, p. 203–211, doi:10.1016/0012-821X(87)90156-7.

Tulloch, A.J., and Kimbrough, D.L., 1989, The Paparoa Metamorphic Core Complex, New Zealand: Cretaceous extension associated with fragmentation of the Pacific margin of Gondwana: Tectonics, v. 8, p. 1217–1234, doi:10.1029/TC008i006p01217.

Tulloch, A.J., and Kimbrough, D., 2003, Paired plutonic belts in convergent margins and the development of high Sr/Y magmatism: Peninsular Ranges batholith of Baja California and Median batholith of New Zealand: Geological Society of America Special Paper 374, p. 275–296, doi:10.1130/0-8137-2374-4.275.

Tulloch, A.J., Ramezani, J., Kimbrough, D.L., Faure, K., and Allibone, H., 2009a, U-Pb geochronology of mid-Paleozoic plutonism in western New Zealand: Implications for S-type granite generation and growth of the east Gondwana margin: Geological Society of America Bulletin, v. 121, p. 1236–1261, doi:10.1130/B26272.1.

Tulloch, A.J., Ramezani, J., Mortimer, N., Mortensen, J., van den Bogaard, P., and Maas, R., 2009b, Cretaceous felsic volcanism in New Zealand and Lord Howe Rise (Zealandia) as a precursor to final Gondwana break-up, *in* Ring, U., and Wernicke, B., eds., Extending a Continent: Architecture, Rheology and Heat Budget: Geological Society, London, Special Publication 321, p. 89–118, doi:10.1144/SP321.5.

Vanderhaeghe, O., and Teyssier, C., 2001, Crustal-scale rheological transitions during late-orogenic collapse: Tectonophysics, v. 335, p. 211–228, doi:10.1016/S0040-1951(01)00053-1.

Verts, L.A., Chamberlain, K.R., and Frost, C.D., 1996, U-Pb sphene dating of metamorphism: The importance of sphene growth in the contact aureole of the Red Mountain pluton, Laramie Mountains, Wyoming: Contributions to Mineralogy and Petrology, v. 125, p. 186–199, doi:10.1007/s004100050215.

White, L.T., and Ireland, T.R., 2012, High-uranium matrix effect in zircon and its implications for SHRIMP U-Pb age determinations: Chemical Geology, v. 306–307, p. 78–91, doi:10.1016/j.chemgeo.2012.02.025.

Whitney, D.L., and Evans, B.W., 2010, Abbreviations for names of rock-forming minerals: American Mineralogist, v. 95, p. 185–187, doi:10.2138/am.2010.3371.

Whitney, D.L., Teyssier, C., and Vanderhaeghe, O., 2004, Gneiss domes and crustal flow, *in* Whitney, D.L., et al., eds., Gneiss Domes in Orogeny: Geological Society of America Special Paper 380, p. 15–33, doi:10.1130/0-8137-2380-9.15.

Wijns, C., Weinberg, R., Gessner, K., and Moresi, L., 2005, Mode of crustal extension determined by rheological layering: Earth and Planetary Science Letters, v. 236, p. 120–134, doi:10.1016/j.epsl.2005.05.030.